

# Irregularity and decadal variation in ENSO: a simplified model based on Principal Oscillation Patterns

Maria Gehne · Richard Kleeman · Kevin E. Trenberth

Received: 11 September 2013 / Accepted: 28 February 2014  
© Springer-Verlag Berlin Heidelberg 2014

**Abstract** A new method of estimating the decay time, mean period and forcing statistics of El Niño–Southern Oscillation (ENSO) has been found. It uses a two-dimensional stochastically forced damped linear oscillator model with the model parameters estimated from a Principal Oscillation Pattern (POP) analysis and associated observed power spectra. It makes use of extended observational time series of 150 years of sea surface temperature (SST) and sea level pressure (SLP) as well as climate model output. This approach is motivated by clear physical relationships that SST and SLP POP patterns have to the ENSO cycle, as well as to each other, indicating that they represent actual physical modes of the climate system. Moreover, the leading POP mode accounts for 20–50 % of the variance on interannual time scales. The POP real part is highly correlated with several Niño indices near zero lag while the imaginary part exhibits a 6–9 month lead time and thus is a precursor. The observed POP power spectra show markedly different behavior for the peak and precursor, the former having more power at ENSO frequencies and the latter dominating at low frequencies. The results realistically suggest a period of oscillation of 4–6 years and a decay time of 8 months, which corresponds to the practical ENSO prediction limit. A fundamental finding of this approach is that the difference between the observed peak and precursor spectra at low frequencies can be related to

the forcing statistics using the simple model, as well as to the difference between patterns of decadal and interannual variability in the Pacific.

**Keywords** ENSO variations · POPs · Spectral analysis · Tropical-extratropical interactions · ENSO predictability

## 1 Introduction

The El Niño–Southern Oscillation (ENSO) climate variation is a coupled ocean–atmosphere phenomenon characterized by anomalous sea surface temperatures (SST) in the eastern to central equatorial Pacific and opposite signed anomalies in the western Pacific with a boomerang shape. Associated with the anomalous SSTs are large-scale sea level pressure (SLP) changes in the tropical Pacific and Indian Ocean. In the developing stage of an El Niño event, changes in SST due to subsurface processes lead to a weakening of the easterly trade winds over the central tropical Pacific which then provides a positive feedback on the initial SST anomalies (Bjerknes 1969). Once a mature El Niño has developed, negative feedbacks are necessary to terminate the event. Although the main signal is located in the equatorial Pacific, ENSO events have important impacts on the global atmospheric circulation (Deser and Wallace 1990; Lau 1997; Alexander et al. 2002). During El Niño events heat stored in the ocean is transferred to the atmosphere directly, mainly in the form of moisture that is eventually released as latent heat through precipitation (Trenberth et al. 2002) and drives changes in energy divergence (Mayer et al. 2013) which in turn drive atmospheric teleconnections (Trenberth et al. 1998). The remote circulation changes due to ENSO can modulate surface fluxes of heat, momentum and moisture through changes in

---

The National Center for Atmospheric Research (NCAR) is sponsored by the National Science Foundation.

---

M. Gehne (✉) · K. E. Trenberth  
National Center for Atmospheric Research, Boulder, CO, USA  
e-mail: mgehne@ucar.edu

R. Kleeman  
New York University, New York, NY, USA

surface temperature, winds and humidity thereby influencing remote ocean properties such as SST, salinity and mixed-layer depth (Alexander et al. 2002). These global responses of weather patterns and extremes make prediction of ENSO events an important task (Chen and Cane 2008; Izumo et al. 2010).

Of particular interest in the prediction of ENSO events is the initiation stage (Chen and Cane 2008). Because sea level height is a precursor for SST (Wyrki 1975) a number of ENSO conceptual models rely on thermocline or subsurface temperature dynamics (Cane and Zebiak 1985; Zebiak and Cane 1987; Jin 1997; Burgers et al. 2005) and communicate the sub-surface variability to the atmosphere through SST anomalies. Observational evidence suggests that the relation among thermocline depth, upper ocean heat content, and SST anomalies is not homogeneous over the equatorial Pacific as it is stronger in the eastern Pacific where the thermocline tends to be shallow (Harrison and Vecchi 2001; Trenberth et al. 2002). There is a long history of studies concerned with ENSO precursors and the evolution of SLP, SST and thermocline depth prior to El Niño and La Niña events both from an observational and a theoretical perspective (Trenberth 1976; Rasmusson and Carpenter 1982; van Loon and Shea 1985, 1987; Trenberth and Shea 1987; Barnett et al. 1988; Trenberth et al. 2002; Stephens et al. 2007). In particular, Penland and Sardeshmukh (1995) identified optimal SST anomaly patterns that lead to El Niño conditions 7 months later. Precursors have been observed in tropical Pacific SST, subsurface temperature, surface wind and sea level height (Weisberg and Wang 1997; Kug et al. 2010) for lead times of about 9 months. Anderson (2003) found evidence of SLP variability in the subtropical North Pacific that can be used to define a precursor index preceding El Niño events by 12–15 months.

Owing to the difficulty of measuring subsurface ocean temperatures, the oceanic component of ENSO is measured by several indices based on SST anomalies in the equatorial Pacific, meanwhile the atmospheric component of this oscillation is commonly measured using the SLP based Southern Oscillation Index (SOI). These indices have three major characteristics: quasi-cyclical behavior, irregularity and a decadal component. A recent review of origins for the irregularity (Kleeman 2008) identifies two main theories: The first assumes that the coupled system is forced by stochastic noise mainly from the atmosphere and this is hypothesized to project significantly onto the coupled dynamical modes and thereby induce ENSO variability (Penland and Sardeshmukh 1995; Thompson and Battisti 2001). This describes ENSO as a stable mode of the coupled system triggered by stochastic forcing. The second theory is based on the idea that nonlinearity in the slow ocean dynamics may induce chaotic behavior and is

thought to occur through the interaction of the annual and ENSO cycles (Chang et al. 1994; Tziperman et al. 1994; Kleeman 2008). In this view ENSO is a self-sustained, naturally oscillatory mode of the coupled ocean-atmosphere system. The question of determinism or stochasticity for ENSO has not yet been resolved, but in a recent study Živković and Rypdal (2013) find that deterministic dynamics of ENSO are primarily associated with the seasonal cycle and that on interannual timescales stochasticity dominates. Similarly, Fedorov et al. (2003) found evidence, based on energetics of ocean-atmosphere interactions, that ENSO is a lightly damped oscillation which is sustained by moderate atmospheric noise. On the other hand, Chen et al. (2004) suggest that the predictability of ENSO depends more on errors in the initial conditions than atmospheric noise, indicating a self-sustained oscillation that is chaotic, but deterministic. Here we will assume that the first mechanism predominates and the implications of such a stochastic perspective are further developed for the cyclical and decadal features of ENSO.

Although quasi-cyclic, an irregular ENSO cycle implies that many frequencies are present, and indeed an analysis of various ENSO measures shows a broadband spectrum peaking around a 4 year period, but with significant power at longer (decadal) periods (Kestin et al. 1998). What is interesting about this decadal power is that a low frequency pass analysis for decadal and longer periods of Pacific SST reveals dominant horizontal modes of variability that differ from the interannual ENSO pattern (Zhang et al. 1997; Kleeman et al. 1999). In particular they show more power in the central rather than eastern equatorial Pacific and also in regions considerably removed from the equator. This pattern is sufficiently distinct from ENSO that it has been referred to as the Pacific Decadal Oscillation (PDO) (Mantua et al. 1997). The PDO broadened to cover the whole Pacific Basin is known as the Inter-decadal Pacific Oscillation (IPO) (Power et al. 1999). The PDO and IPO exhibit virtually identical temporal evolution (Folland et al. 2002). The precise connection of the decadal and dominant interannual Pacific ENSO climate variability remains unclear and is a topic of active research as there is evidently significant commonality of horizontal structure and global effects (Newman et al. 2003; Vimont 2005).

A recently proposed explanation for this connection derives from stochastic theory. Kleeman (2011) derive a framework for analyzing the spectrum of a general multi-dimensional Ornstein-Uhlenbeck process. This framework allows the explicit evaluation of the spectrum in terms of the normal mode frequencies, dissipation and the stochastic forcing statistics. In this paper we further explore the conceptual model proposed in Kleeman (2011) by applying the framework to ENSO variability as identified by a Principal Oscillation Pattern (POP) analysis of SST and

SLP data. We show that the POP time series of the leading mode can be categorized as a peak and precursor for ENSO and that they have the observed characteristics of quasi-cyclical behavior, irregularity and decadal variability. We show that the difference between interannual and decadal patterns can be related to the precursor having more power at decadal frequencies than the peak, and the peak dominating at interannual frequencies.

The approach proposed here uses the analytical connection between model parameters and power spectra to robustly estimate ENSO decay time and period. Section 2 introduces POPs and the methods of analysis, along with the data sets used. Section 3 describes the patterns and time series obtained from the POP analysis. The stochastic model is outlined in Sects. 4, and 5 describes how the model parameters are selected, given the observational results. Section 6 places the results and the model in context and gives the main conclusions. Details outlining the sensitivity of results to the data sets used, domains and periods, the mathematical formula for the forcing for the stochastic model, the derivation of the theoretical spectra, as well as how the peak and precursor time series are computed are included in the “Appendix 1–4”.

## 2 Methods and observational data

Observational time series of sufficient duration are necessary to enable a stable spectrum to emerge (Kestin et al. 1998). When using time series of only 5 ENSO periods (20 years) the spectra are not stable and are sufficiently affected by sampling variations that non-robust spectral peaks may occur. When one chooses data of length around 100 years, i.e. 25 ENSO periods, however, this problem is considerably reduced. In that case non-stationarity of the climate record becomes an issue. The implications this has on the results presented here are discussed in Sect. 3. Long time series of both the dominant ENSO pattern and its precursor, which is identified via POP analysis as described below, are therefore required. The time series associated with the dominant ENSO pattern has been widely studied but the precursor pattern presents problems since it has considerably less variance in the SST and SLP records. However, the precursor pattern is particularly evident in ocean dynamical height or thermocline data but such data are not available in the regions needed for 100 years. SST data sets have better coverage generally due to COADS ship reports but there remain significant issues in the tropical Pacific before 1950, and often such data sets rely on global reconstruction techniques to infer tropical data from correlated extratropical data (Meyers et al. 1999). Finally the SLP precursor data discussed rely on station barometric data which can have long term coverage for

several sites (Allan and Ansell 2006). In general SLP station data might be expected to provide better long term data than ship reports of SST which only became common (and of reasonable quality) in the tropical Pacific in the postwar period. Both SST and SLP data are used in the analysis presented here.

The peak phase of ENSO is commonly measured by SST index regions such as Niño3 (90°W–150°W, 5°S–5°N) and by the SLP derived SOI. Monthly values are available from the IRI/LDEO Climate Data Library for Niño3 from January 1856 through March 2011 and for the SOI from January 1882 through December 1996. SOI data prior to 1935 are based on data from Darwin only. The results presented are not sensitive to the use of either index. In order to calculate time series for the precursor pattern, a POP analysis on long term monthly, global SLP and SST data sets is performed. Results presented are based primarily on SST from the Hadley Centre 1° sea ice and SST data set (HadISST) (Rayner et al. 2003) available from 1870 to 2012 and SLP from the 2° NOAA twentieth century reanalysis (20CRSLP) (Compo et al. 2011) from 1871 to 2012. The analyses have been performed on multiple other data sets as well to check consistency of the results among data sets (see “Appendix 1”).

Principal Oscillation Pattern (POP) analysis is a technique used to identify oscillatory patterns and space-time characteristics of complex systems (Storch et al. 1988, 1995). POPs are the normal modes of a linear system, where the system matrix is estimated from observational data. The leading POPs can be shown to correspond to the most unstable modes of the linearized system (Storch and Zwiers 1999). POP analysis has been used extensively in the context of studying ENSO mechanisms (Xu and Storch 1990; Penland and Magorian 1993; Latif et al. 1994; Wu et al. 1994). The leading oscillatory mode obtained from a POP analysis of SST or SLP describes the spatial patterns and variability associated with ENSO. This mode is complex and describes a propagating pattern that can be represented by two standing modes varying in quadrature.

The computation of SLP and SST POP analyses follows the technique documented in Storch et al. (1995) and Storch and Zwiers (1999). The mean annual cycle is calculated using the entire length of the time series and removed to obtain anomalies. The region for the analysis contains the Indian and Pacific Ocean (45°E–70°W) between 40°S and 40°N and the full length of the time series for SLP and SST anomalies is used. The specific analysis technique was performed following Xu and Storch (1990). The primary analysis emphasizes the large scales and accordingly uses a spatial resolution of 10° in the meridional and 20° in the zonal direction, but results can be projected onto higher resolution grids. A linear trend is removed before the data are normalized at each grid point

by the local standard deviation to take into account the difference in variability between midlatitudes and tropics. Short time scale variance (less than 15 months) is removed and time scales longer than 18 months are kept with a cosine taper in frequency space between these limits. POPs are computed on the subspace spanned by the projection of the data onto the first 10 Empirical Orthogonal Functions (EOFs). Experiments show that the results are stable for POP 1 when using at least 9 EOFs and for the first 3 POP pairs when using at least 10 EOFs. The patterns and time series are not very sensitive to the choice of the domain size. Decreasing the meridional extent of the domain to  $\pm 20^\circ$  and  $\pm 10^\circ$  does not change the POP time series and power spectra substantially (this issue is further discussed in Sect. 6).

### 3 Results of POP analysis

For illustration the first 2 POPs of SST and SLP are shown in Fig. 1 (HadISST and 20CrSLP), but, in the following, the focus is on the dominant POP pair. The real and imaginary parts of the spatial patterns are denoted by  $(P_{r,i}^{\text{slp}}, P_{r,i}^{\text{sst}})$  and the corresponding time series by  $(z_{r,i}^{\text{slp}}, z_{r,i}^{\text{sst}})$ . There is good agreement among the data sets with regard to the first POP spatial patterns in SST and SLP for both real and imaginary parts.

The sign of the patterns and time series identified by a POP analysis is arbitrary. The signs of the time series are set so that  $z_r^{\text{sst}}$  and  $z_r^{\text{slp}}$  are positively correlated with the Niño3 index and the imaginary parts are positively correlated with Niño3 prior to an El Niño event. This determines the signs of the spatial patterns and the real and imaginary part of the dominant POP are referred to as peak and precursor phase of ENSO respectively. Time series associated with the first POP real and imaginary parts (Fig. 1) reveal that the peak time series clearly show the recent large ENSO events: the 1972–1973, 1982–1983, 1986–1987 and 1997–1998 El Niños in addition to the immediately following La Niña episodes. For these large events the precursor time series peaks several months before the peak and changes sign after the peak phase maximum. The time series also show a decrease in variance between 1930 and 1960 and with the most vigorous variability appearing during the most recent decades (Trenberth 1976; Wang and Wang 1996; Kestin et al. 1998; Torrence and Compo 1998; Torrence and Webster 1999). Peak and precursor phase during large events are in quadrature, whereas this relationship becomes weaker at other times. Especially during the period of weak variability, the quadrature relation breaks down. For all data sets and both SST and SLP the precursor variance is

maximized in June whereas the peak variance has a maximum in November/December.

For POPs 2 (and 3, not shown) the correspondence between data sets is not as good, especially in SLP, and there appears to be no clear physical connection between real and imaginary parts. The one exception being the real part of POP 2 which shows a PDO type pattern with meridionally broad positive SST anomalies in the eastern equatorial Pacific and negative SST anomalies in the central off-equatorial Pacific. Unlike the peak ENSO signal, where the positive anomalies in the equatorial region are much stronger, POP 2 has the tropical and off-equatorial anomalies of comparable magnitude. The associated SLP signal is a strong low pressure node in the northern Pacific, which can be identified in the POP 2 real part in Fig. 1. The imaginary part of the POP 2 pattern has very little signal in the Pacific indicating that POP 2 describes a standing wave rather than a propagation. Note that the real parts of POP 1 and POP 2 pattern are not orthogonal to each other in the Pacific, but that the signal in the Indian and Atlantic Ocean is very different.

#### 3.1 Reconstruction of 1997–1998 El Niño

To illustrate the behavior of the first POP mode, Fig. 2 shows the evolution of the 1997–1998 El Niño event SST and SLP anomalies reconstructed using the first POP patterns and time series. In January to March 1997 low SST anomalies in the western Pacific and low pressure nodes in the subtropical central Pacific are visible with little or no positive SST signal in the eastern equatorial Pacific. By May 1997 the eastern equatorial SST anomalies are positive and growing. Concurrently negative SLP anomalies in that region are strengthening while the subtropical low pressure node moves farther east and poleward. From September 1997 to January 1998 the tropical anomalies are maximized while the negative SST anomalies in the northern central Pacific are still strengthening, along with a strengthening of the north Pacific low pressure center. Starting in March 1998, the anomalies weaken and the high pressure over the maritime continent develops into two high pressure nodes that move east and north towards the central subtropical Pacific regions. By September 1998 both SLP and SST anomalies are weak, with small positive SST anomalies in the western and small negative SST anomalies in the eastern equatorial Pacific.

#### 3.2 Physical relevance of the POP modes

Referring to the time series as peak and precursor for ENSO implies that the leading POP modes are relevant physical modes in the ocean atmosphere system. However, a POP analysis does not necessarily identify intrinsic

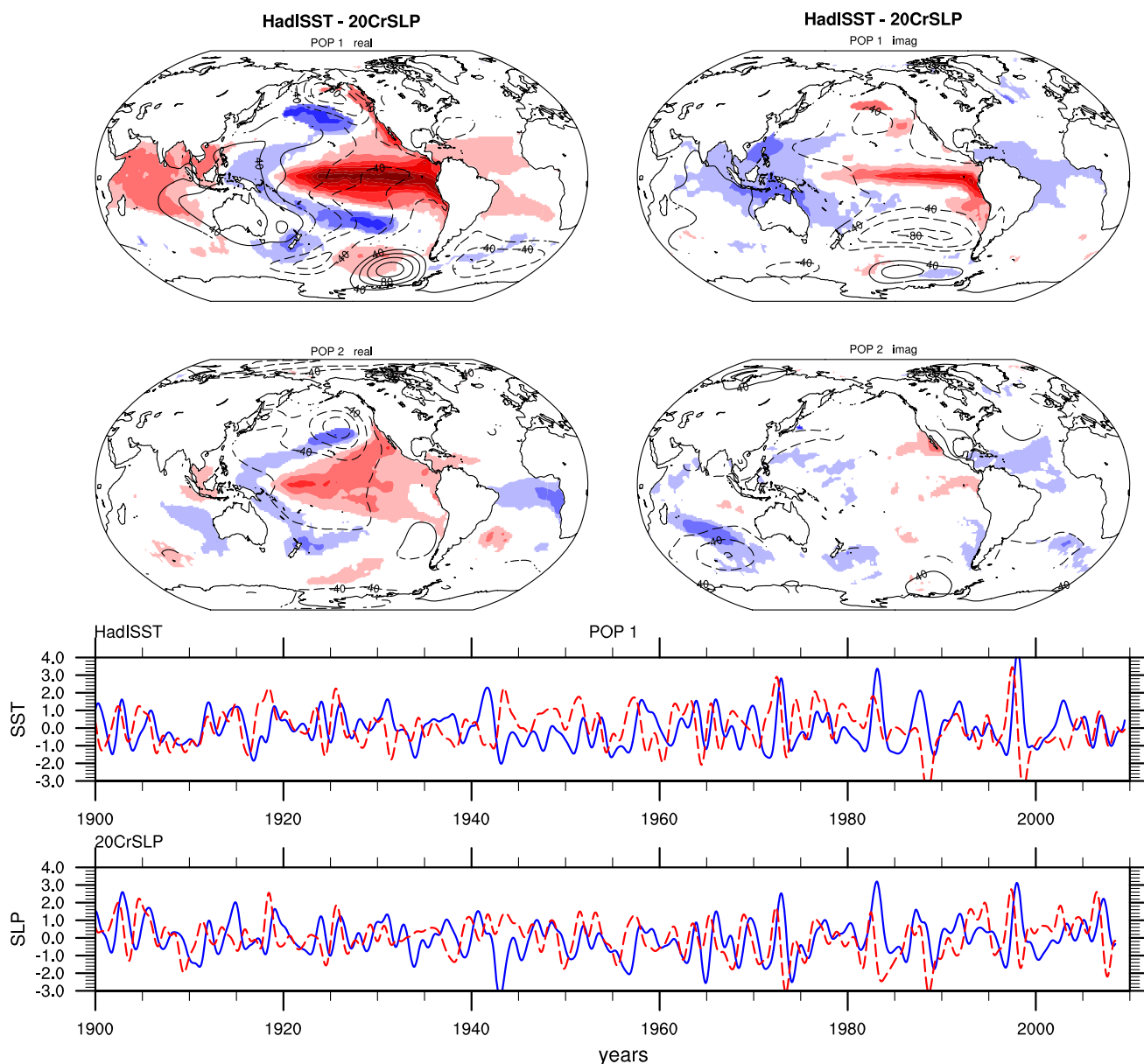


**Fig. 1** HadISST (*shading*) and 20CrSLP (*contours*) patterns of the first 2 POP pairs and POP1 time series. The real part in the *top left panel* corresponds to the mature phase of ENSO and has a strong positive SST signal in the eastern equatorial Pacific and a weaker positive signal in the Indian Ocean. These positive anomalies are separated by a weaker (comparable to the anomaly in the Indian Ocean) negative anomaly stretching from the western equatorial to the central subtropical Pacific. The imaginary part in the *top right panel* corresponds to the ENSO precursor pattern and has a weaker SST signal confined mainly to the maritime continent region. Overlaid are contour lines of HadSLP POP real and imaginary parts

respectively. The mature ENSO signal shows the well-known low pressure in the eastern and high pressure in the western Pacific. The precursor signal shows two low pressure systems in the central off-equatorial Pacific. Units are K/SD for SST (*shading*) and Pa/SD for SLP (*contours*). Shading starts at 0.05 with contour intervals of 0.1. Contour lines and shading are statistically significant at the 95 % limit. POP1 time series for HadISST (lower panels, *top*) and 20CrSLP (lower panels, *bottom*). Each panel shows time series for the peak or real part (*blue solid*) and precursor or imaginary part (*red dashed*). Time series are normalized to have zero mean and unit variance

modes of climate variability. Clear physical interpretation, of the precursor phase in particular, is therefore necessary to justify using these modes.

The SST precursor signal identified by the POP analysis in the western equatorial Pacific is located in a region with

little variance. The precursor has very little amplitude compared to the peak pattern, although the regressions are significant at the 95 % confidence level. The relatively small amplitude raises the issue of whether the sparse and inaccurate observations in the early part of the record are

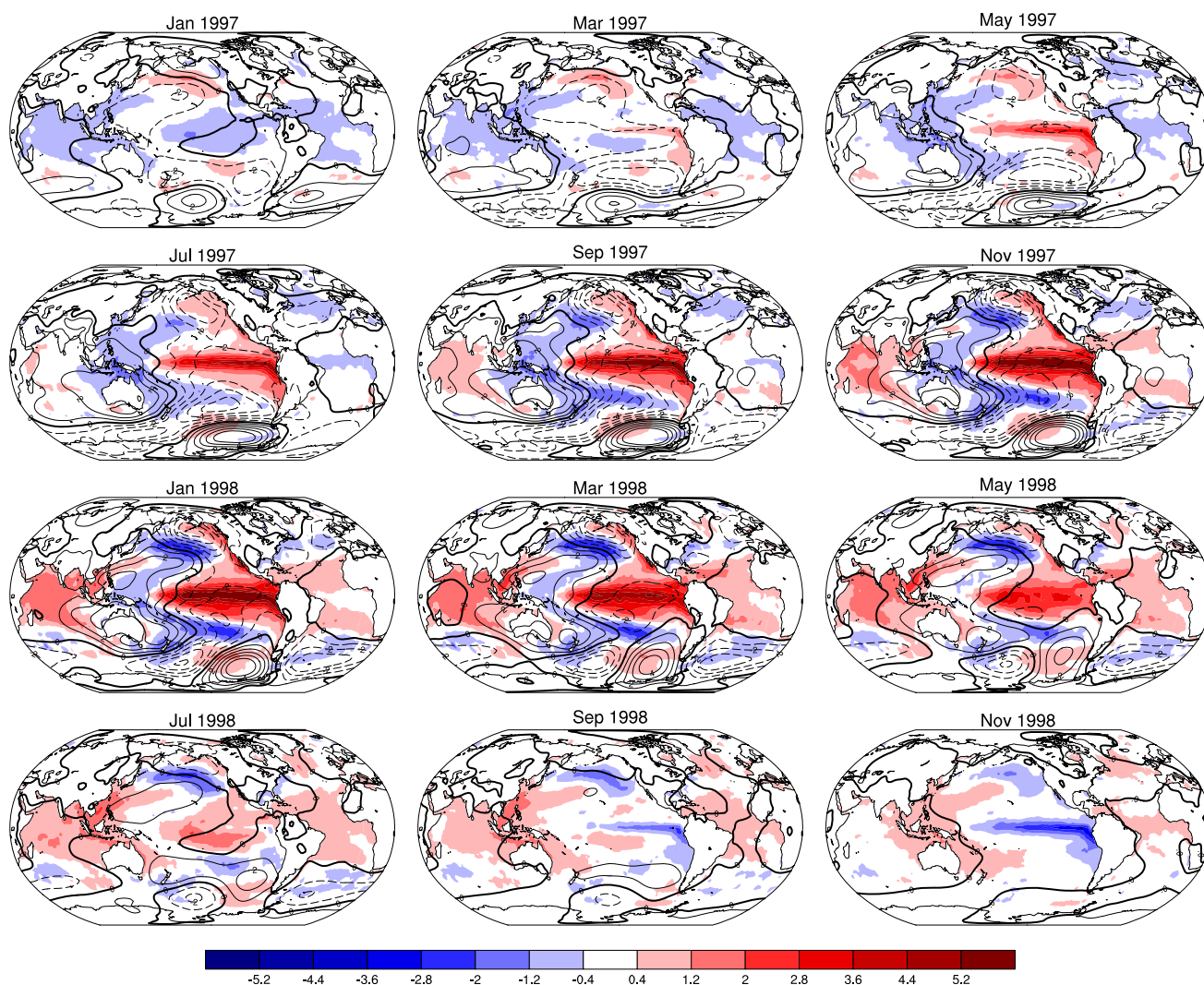


**Fig. 2** Reconstruction of SST (*shading*) and SLP (*contours*) anomalies during 1997–1998 using HadISST and 20CrSLP POP1. Panels are snapshots of the reconstructed anomalies as captured by the first POP pair starting in January 1997 every 2 months until November

1998. Units are K for SST and hPa for SLP anomalies. SLP contour intervals are 2 hPa and negative contours are dashed, the zero contour is marked by the *thick line*

able to adequately capture the signal. However, even though the SST precursor pattern explains little variance of the climate system, it may still be an important component of ENSO evolution. In addition, all SST data sets agree on the precursor signal in the western Pacific, indicating that reconstructions do pick up the small amplitude signals in this region. The stability of the POP analysis results with respect to the data period used is tested by computing the first POP pair and spectra for the common data period 1871–1997. The same spectra were computed excluding the first or last decade of that range (periods 1871–1987 and 1881–1997). The POPs and spectra for the different periods show very similar behavior at ENSO periods indicating that small changes in the data period do not lead to large changes the results. The low frequency part of the

spectrum does show some variance between the periods, depending on the dataset, but not enough to be qualitatively different (not shown).

The SST precursor has most of its signal in the western equatorial Pacific, with negative SST anomalies extending northeast from the western tropical Pacific flanked by positive SST anomalies. The SLP precursor consists of two low pressure nodes in the central North and South Pacific. Note the asymmetry in the strength of the low pressure nodes, the southern hemispheric node is stronger and has a larger zonal extent than the northern hemispheric node. This illustrates the fact that the southern hemisphere plays a major role in the atmospheric component of ENSO. The precursor SLP anomalies identified by the POP analysis in the south central Pacific are consistent with the anomalies

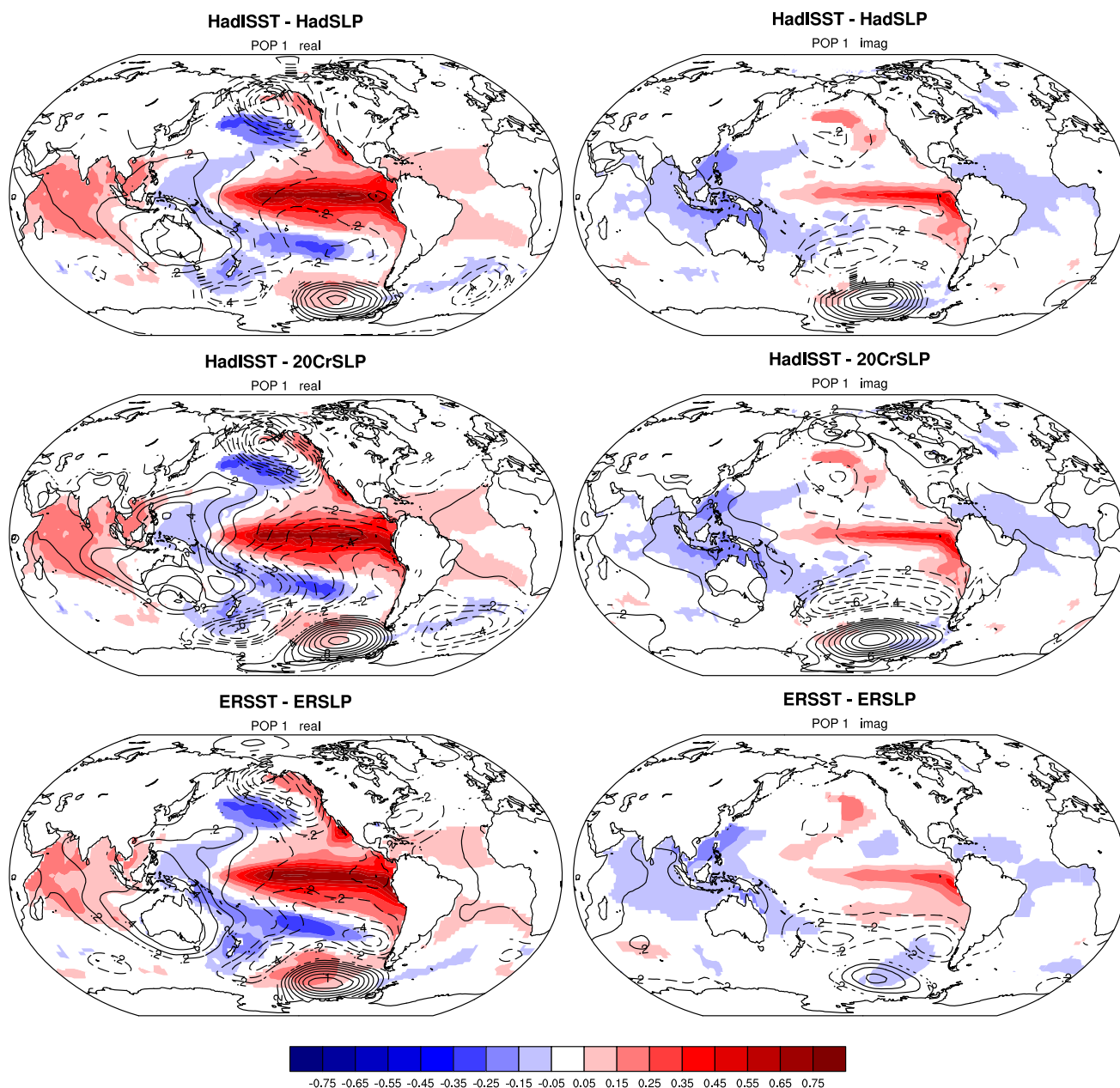


**Fig. 3** SLP regression pattern on SST POP1 time series for different data sets. *Shading* shows the SST regression patterns on SST POP1 time series, *contours* show SLP data regressed on SST POPs. Peak phase (*left panels*) and precursor phase (*right panels*). *Panels* are

labeled by the SST and SLP data sets used for the regression. Units are K/SD for SST (*shading*) and hPa/SD for SLP (*contours*). *Contour lines* and *shading* are statistically significant at the 90 % limit. These should be compared with *top panels* of Fig. 1

observed by van Loon and Shea (1987). These two low pressure nodes identified by the POP analysis are also the atmospheric patterns corresponding to the precursor SST variability. This can be seen from Fig. 3 which shows the SST peak and precursor patterns and the SLP regression patterns onto  $z_{r,i}^{sst}$ . Comparison of the POP 1 patterns in Fig. 1 and the regression patterns in Fig. 3 shows that the SLP POP analysis evidently identifies an SLP precursor connected to the SST POP precursor. The fact that SLP and

SST precursors can be identified from separate data sets and the results match regression patterns of one of the time series on the other increases our confidence that these are actual modes in the system and not a product of the reconstruction techniques.

The location of the low pressure systems to the east of anomalous low SST in the precursor is consistent with the idea that during the onset of El Niño conditions, westerly wind bursts are more common in the western equatorial Pacific

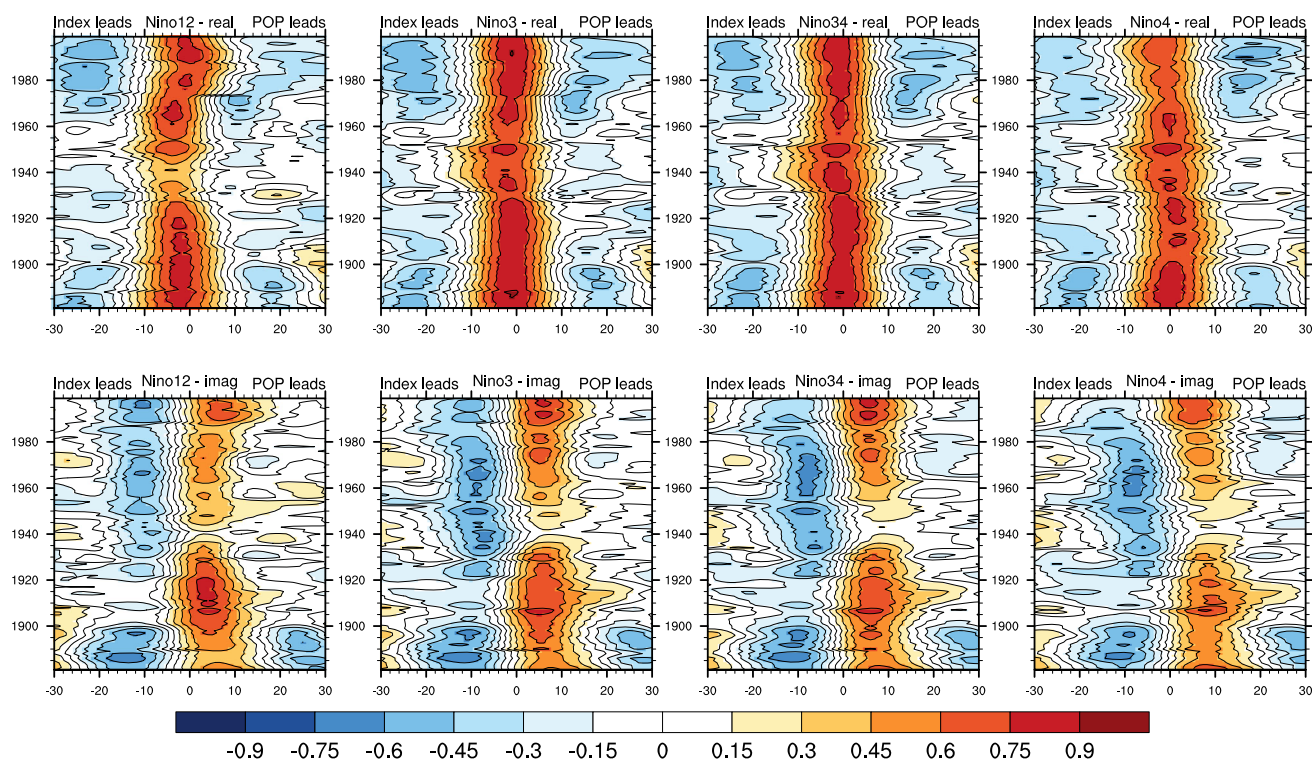


**Fig. 4** Lag correlations of 21 year time segments between Niño indices and HadISST POP1 real and imaginary parts. Lag correlations for each 21 year window are labeled by the center year of the window. Positive lags imply that the index lags the given time series,

negative lags mean the index leads. *Top panels* show correlation with the peak, *lower panels* show correlation with the precursor. Results for the other data sets are similar but are not shown

leading to more mixing in the upper ocean and a deepening and cooling of the mixed layer (Lukas and Lindstrom 1991). This cooling in SST along the western boundary of the equatorial Pacific shifts the warmest ocean temperatures eastward and with that the region of most vigorous convection leading to the development of anomalous low pressure systems in the central Pacific. The same anomalous SST gradient results in a positive feedback, as it favors westerly wind anomalies (Delcroix and McPhaden 2002). The precursor SST patterns also compare well with the optimal initial SST perturbations of Penland and Sardeshmukh (1995) that evolve into El Niño conditions within 7 months.

The precursor SST and SLP patterns are also consistent with the seasonal footprinting mechanism proposed by Vimont et al. (2003a, b), whereby winter SLP anomalies (like the precursor shown here) the year prior to an El Niño event generate mid-latitude and subtropical SST anomalies (negative SST anomalies in the western subtropical Pacific consistent with the SST precursor) through changes in the surface heat fluxes. The SST anomalies persist into boreal summer where these anomalies feed back on the atmospheric circulation and generate zonal wind stress anomalies that extend to the equator. These wind stress anomalies can then lead to an El Niño event. Consistent with this are

the lag correlations of the peak and precursor time series with several Niño indices shown in Fig. 4. Both SST and SLP precursors have maximum positive correlation with the Niño indices at 5–9 months prior to an El Niño event and negative correlation several months after. The maximum correlations occur about 3 months earlier for SLP (not shown) than for SST indicating that the SLP precursor slightly leads the SST precursor in their relation to the Niño indices. During the decay of an El Niño event there is an overshoot of SST anomalies in the eastern tropical Pacific to negative values, consistent with the negative SST precursor pattern. There is substantial variability in the relationship between the Niño indices and the POP time series over the length of the data record. From 1930 to 1960, when ENSO variability was reduced, the peak correlation values decrease in the precursor to values below 0.3. The lag at which maximum correlations are obtained also varies over time, more than between indices. Maximum correlation between peak and Niño4 time series is achieved at zero lag at the beginning of the record and at negative 2 months lag in recent years (such that the peak lags Niño4 by 2 months), whereas the timing of maximum correlation stays relatively constant at negative 1–2 months for the Niño3 and Niño3.4 indices.

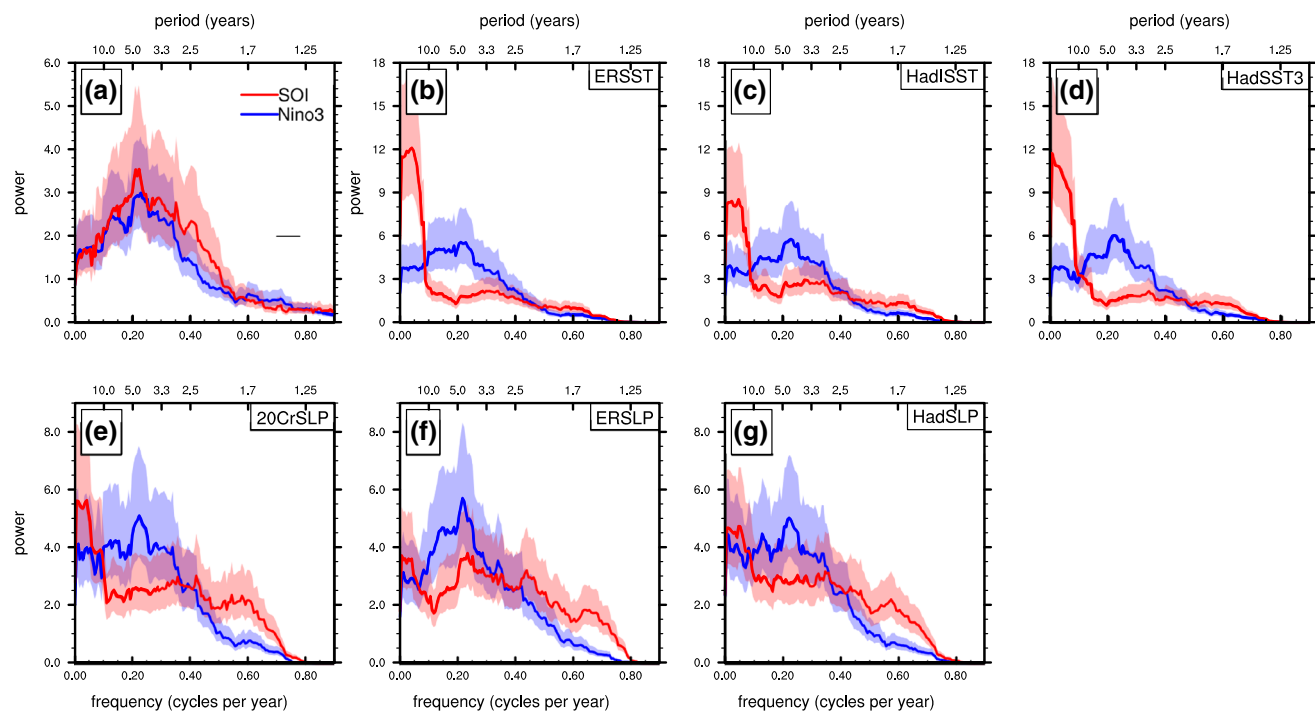


**Fig. 5** Observed power spectra of the first POP pair. **a** Niño3 and SOI power spectra. **b–g** Peak ENSO (blue) and precursor (red) power spectra of the standardized time series for the different data sets. The shading shows the 90 % confidence intervals. All spectra are computed using the Thomson Multitaper method, with the effective bandwidth indicated by the horizontal line in the top left panel. The

area under the curve is 1.9 for the POP spectra and the Niño3 and SOI spectra are not normalized to have the same area under the spectral curve. The area under the curve is computed for the entire spectral curve, but only the values up to 0.9 cycles per year are shown as the spectra are essentially zero for higher frequencies

We have shown that POP analysis identifies physically relevant modes of SST and SLP variability. POP 1 does not describe the full ENSO dynamics, but it has relevant physical meaning and is responsible for a high percentage of the variance on interannual time scales. POP 1 accounts for 20–50 %, depending on the data set (higher for SST than SLP), of the variance of the interannual part of the data. It is therefore worthwhile to consider this mode further and analyze its characteristics.

### 3.3 Power spectra

Spectra for both POP 1 time series for SLP and SST data were computed using the Thomson Multitaper method (Percival and Walden 1998; Thomson 1982). Figure 5 shows the power spectra for POP 1 for the different data sets considered, as well as the Niño3 and SOI spectra. The spectra for all  $z_r^{\text{slp}}$  and  $z_r^{\text{sst}}$  (the peak ENSO phase) have very similar characteristics to the Niño3 spectrum. The main peak is at a period of about 4 years with a strong decay at higher frequencies and a smaller rolloff at lower decadal frequencies. The  $z_i^{\text{slp}}$  spectrum, i.e. the ENSO precursor, on the other hand has less maximum power and the ratio of ENSO peak power to decadal variability is noticeably smaller, and this phase

has relatively greater decadal weight. There is also more power for periods between 1.25 and 2.5 years in the precursor spectrum compared with the peak spectrum. There is very good agreement among all data sets and between SST and SLP derived spectra, with the former having more power at low frequencies in the precursor.

The aim is to use the power spectra estimated from observations to identify model parameters for a 2D model introduced in Sect. 4, therefore an assessment of the degree of uncertainty associated with the spectral estimates is useful. One way is shown in Fig. 5 by the 90 % confidence intervals. However, this does not take into account the fact that the short 150 year data record may not represent the full variability of the coupled climate system. In an attempt to better understand possible variability in the power spectra, long control runs of two Coupled Model Inter-comparison Project 5 (CMIP5) models: the CCSM4 (Deser et al. 2012) and ECHAM6 (Stevens et al. 2013) models are used. These models have reasonable ENSO variability and the patterns obtained by the POP analysis of the control runs are similar to observations (not shown). The control runs are 1300 and 1000 years long for CCSM4 and ECHAM6 respectively. To compare to the observational record, the SST and SLP records are split into non-

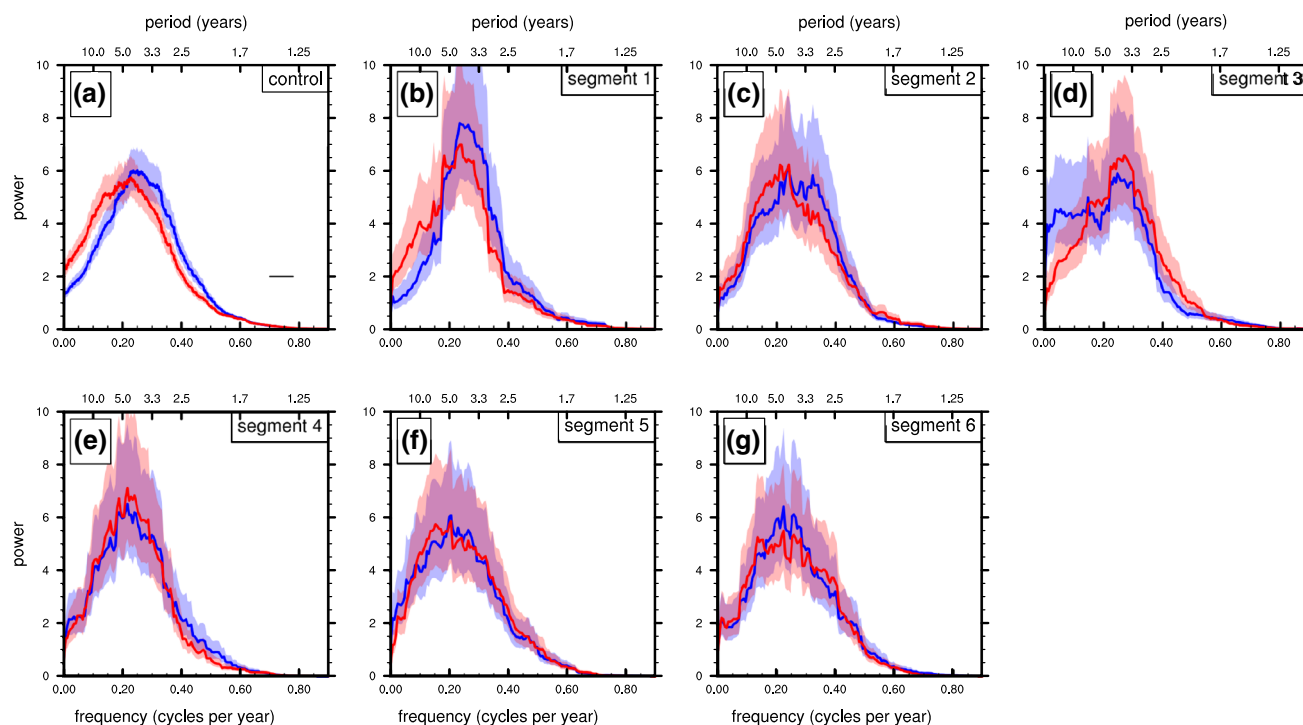


**Fig. 6** ECHAM model SST POP spectra for **a** the low resolution control run and **b–g** 6 not overlapping 150 year segments. *Different colors in each panel* are for peak and precursor spectra. Peak and precursor spectra do not necessarily have the same color in different

panels or as in Fig. 5. *Shading* shows the 90 % confidence intervals. POPs are computed as for observations and all spectra are computed using the Thomson Multitaper method

overlapping 150 year segments and the leading POP modes and their spectra are calculated for each segment separately, in addition to computing the spectra for the whole length of the model runs. Figure 6 shows the segment spectra for the ECHAM6 control run. Results from CCSM4 SST and SLP are similar. It is clear that the spectra do vary among segments with one of the spectra (the peak spectrum) varying only slightly and the other changing considerably; in some segments both spectra are essentially identical and at other times the resemblance to observations (Fig. 5) is stronger. The spectra from the full 1000 (1300) year runs resemble the observed peak spectra with only small differences between modeled peak and precursor at low frequencies (Fig. 6a). Some of the modeled climate states of ENSO identified through the POP analysis are consistent with the observed power spectra. This suggests that although the data record is short compared to the ENSO oscillation period, in the sense that a sample size of 30–35 ENSO events is small for adequately resolving the ENSO spectral peak, the peak spectrum is well estimated from the data record and the precursor spectrum is at least a possible scenario.

The changes in precursor spectra observed in the two CMIP5 models indicate that over longer time spans than the

observational record, different precursor mechanisms can be important during different time intervals. If both peak and precursor spectrum have a well defined peak at the oscillation frequency with the same power then the system is closer to a regular oscillation with added noise. If one of the phases has less power at the oscillation period (and possibly more power at other frequencies) not every El Niño event needs to be preceded by the precursor identified by the POP analysis, but rather other mechanisms are more important than in the case where both spectra are the same. In that case the oscillation would be more similar to a standing wave than a propagating wave. Evidence of a precursor to ENSO with varying influence over time was recently described by Anderson et al. (2013). They found that variations in SLP in the northern central Pacific 12 months prior to an El Niño influences the asymmetry between El Niño and La Niña events, and that there are time periods where ENSO variability is not tied to this particular precursor.

### 3.4 Decadal variability of the POP modes

What is the source of the decadal power in the precursor spectrum? The correlation between the precursor and the PDO index (Mantua et al. 1997) is 0.64, and 0.1 for the

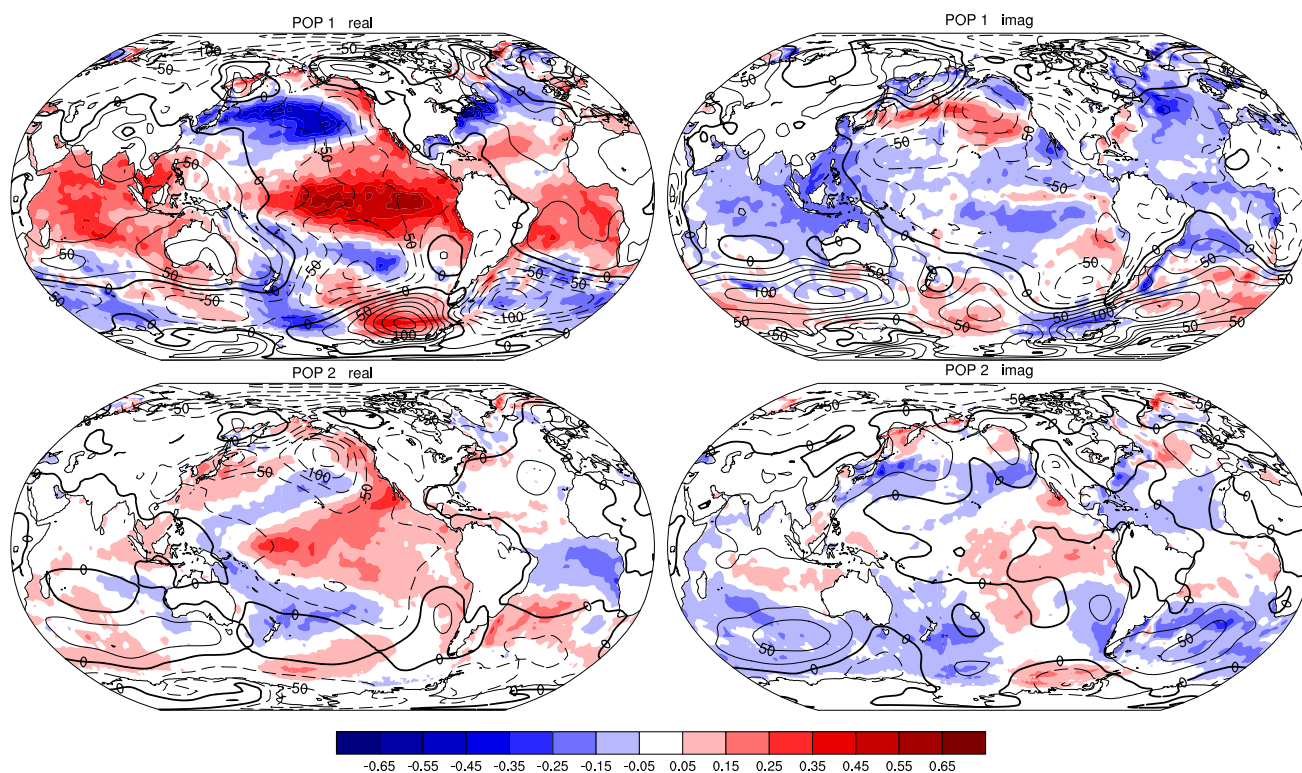


**Fig. 7** Regression patterns of low pass filtered HadISST and 20CRSLP and the corresponding low pass filtered POP 1 and POP 2 time series. Decadal frequencies are isolated using a low-pass filter

for time scales longer than 8 years. Units are K/SD for SST (*shading*) and Pa/SD for SLP (*contours*)

peak phase, both significant at the 95 % level. Filtering for decadal time scales increases the correlation to 0.7 and 0.4 for precursor and peak respectively. The covariability between precursor and PDO suggests there may be similar processes involved in generating the decadal variability of precursor and PDO. Reducing the domain latitudinal extent from  $\pm 40^\circ$  to  $\pm 20^\circ$  and  $\pm 10^\circ$  shows that the decadal power in the precursor does not decrease with decreasing latitude band, especially in SST (not shown). This may indicate an equatorial source for this peak. In addition most of the variability and a quadratic trend of the low pass filtered (for decadal frequencies, see below) precursor time series can be recovered from the low pass filtered average of SST anomalies in the western equatorial Pacific ( $10^\circ\text{S}$ – $20^\circ\text{N}$ ,  $120^\circ\text{E}$ – $150^\circ\text{E}$ ). It appears likely that the decadal variability of the precursor may be driven to a certain degree from western equatorial Pacific SST anomalies. To investigate in detail the origin of western equatorial Pacific SST decadal variability is beyond the scope of this study, however a number of theories exist for the physical mechanisms that drive western Pacific SST decadal variability. Ocean dynamics play a role in driving the formation and variability of the warm pool, in particular advection of upper-ocean temperatures by mean and anomalous ocean currents (Wang and Mehta 2008) and variability of shallow tropical

circulations (Lohmann and Latif 2005) have been suggested.

How much of Pacific decadal variability is captured by the interannual part of the POP modes? Following Vimont (2005) both SST and SLP data sets and the POP time series are low-pass filtered for decadal frequencies. A 193 point (16 year) low-pass Lanczos filter is used on the monthly time series with a half-power point at 0.12 or 8.3 years. Figure 7 shows the regression patterns of the decadal part of the time series for POP 1 and 2. POP 1 real part shows a pattern associated with the PDO, with meridionally broad positive SST anomalies in the eastern and central Pacific and negative anomalies in the north Pacific. The corresponding SLP pattern shows the Aleutian low for POP 1 and strong signals in the southern Pacific ocean. POP 2 real part shows an SST and SLP patterns similar to the one associated with the central Pacific warming ENSO signal and the North Pacific Gyre Oscillation (NPGO) (Lorenzo et al. 2010). The POP 1 SST imaginary part shows an overall weaker signal than the real part and is largely of opposite sign, the main differences are in the northern Atlantic and tropical eastern to central Pacific ocean. The POP 2 imaginary part is less easily interpreted.

The interannual part is defined as the difference between the full data and the decadal part. In terms of SST we

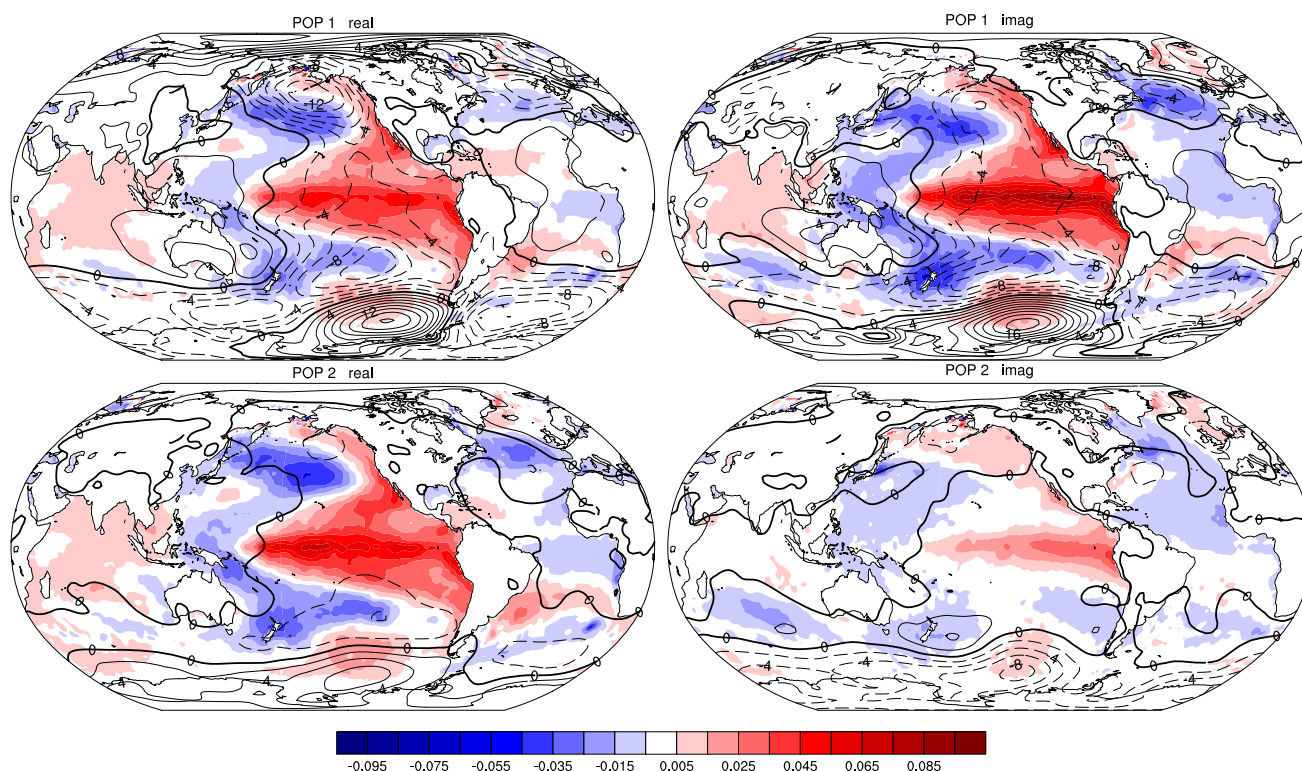


**Fig. 8** Regression patterns associated with the decadal variability of the interannual POP 1 and POP 2 patterns for HadISST and 20CRSLP. Decadal variability associated with interannual patterns is found by projecting the full data onto the interannual POP patterns. This results in time series associated with the interannual patterns.

The time series are then filtered for decadal frequencies and regressed onto the data filtered for interannual time scales. These patterns describe the decadal variability generated by the interannual patterns. Units are K/SD for SST (*shading*) and Pa/SD for SLP (*contours*)

denote the interannual part by  $SST^H$  for the data,  $Z_{SST}^H$  for the POP time series, and  $POP^H$  for the patterns. The interannual patterns are obtained by regressing  $Z_{SST}^H$  against  $SST^H$ . The full (interannual and decadal) SST data are then regressed against the interannual patterns  $POP^H$  and the resulting time series are filtered for decadal frequencies. The filtered time series are denoted by  $pZ_{SST}^H$  and describe the decadal variability associated with the interannual POP patterns. Regression of interannual  $SST^H$  against these time series give the spatial patterns associated with the decadal variability generated from interannual processes (Vimont 2005). In the decadal spatial patterns reconstructed from the decadal variability of the interannual patterns (Fig. 8), both real and imaginary part of POP 1, i.e. the peak and precursor for ENSO, show similar decadal patterns with a broader meridional structure than the interannual peak ENSO pattern, and similar magnitudes for the positive and negative anomalies at the equator and midlatitudes respectively. Both interannual spatial patterns are needed to capture the decadal variability. SLP decadal variability is captured by a low pressure node over the northern North Pacific and another one over the central South Pacific with high SLP anomalies over the western equatorial Pacific and

Indian Ocean. The SLP anomalies are stronger for the peak decadal pattern than for the precursor. The POP 2 SST real part is very similar to the POP 1 patterns, but the connection to the POP 2 SLP pattern is less clear. The imaginary part shows a warming in the southern hemisphere and cooling in the north. The main SLP signal in POP 2 is an oscillation in circumpolar SLP anomalies, which may be related to the Southern Annular Mode.

The above arguments show that the interannual patterns of the first POP generate decadal variability consistent with observed decadal variability in the Pacific and implies that the simple model, through the peak and precursor spectra, is able to produce realistic decadal variability.

## 4 Theoretical model

### 4.1 2D model and spectrum

In Kleeman (2011) a simple two component stochastically-forced damped oscillator is suggested as a minimal model for ENSO. The simple model described here is able to reproduce the cyclic and irregular behavior of ENSO quite

well. We show that if in addition the stochastic forcing of the two phases is either correlated to a small extent or else of differing magnitude, then there is a significant cross-spectral contribution to the power spectrum and this can be related to decadal variability. As such forcing statistics seem likely to some degree, such a model is an interesting one to explore in detail. The existence of long data sets of the two phases discussed in the previous section suggests that an observational fitting exercise might be productive, particularly since some of the model parameters have an important physical interpretation. For example, the damping time of the oscillator can be directly related to the predictability limit of ENSO (Kleeman 2011). Thompson and Battisti (2001) shows that the red decay and prominent spectral peak of the observed Niño3 spectrum is reproducible qualitatively using the minimal model. Here, the model is extended to include the precursor phase and fitting exercise for the simple model is performed using the two observed spectra.

The discussed two component model can be written as the following linear stochastic differential equation:

$$d \begin{bmatrix} x \\ y \end{bmatrix} = \mathbf{A} \begin{bmatrix} x \\ y \end{bmatrix} dt + \mathbf{F}dW, \tag{1}$$

where

$$\mathbf{A} = \begin{bmatrix} \varepsilon & -\eta \\ \eta & \varepsilon \end{bmatrix} \tag{2}$$

with  $\mathbf{F}$  the forcing matrix and  $W$  the (vector) Wiener stochastic process. This equation represents a stochastically forced linear damped oscillator with  $\varepsilon = \frac{1}{\tau}$  where  $\tau$  is the damping time and  $\eta = \frac{2\pi}{T}$  with  $T$  the period of the oscillation. This model can also be interpreted as the dominant normal mode with the least damping in the system, or the normal mode with the largest projection of stochastic forcing. The two components of the model can be thought to correspond to the first two EOFs of ocean heat content (and their associated patterns in other physical variables). As noted earlier, modes with these characteristics can be identified in data via POP analyses (Storch et al. 1988; Kleeman and Moore 1999). Note that the two orthogonal phases of the POP are here being represented by standard orthogonal unit vectors. Similar models have been proposed before without the stochastic forcing term (Xu and Storch 1990) and with stochastic forcing but considering multiple normal modes (Penland and Sardeshmukh 1995).

The stochastic forcing in Eq. (1) has an associated covariance matrix  $\mathbf{R}$  which represents the forcing in terms of the two phases. This contains as parameters the variance of the forcing on the two phases as well as the correlation between them. It can be written as

$$\mathbf{R} = \mathbf{F}\mathbf{F}^T = c \begin{bmatrix} 1 & r\sqrt{\alpha} \\ r\sqrt{\alpha} & \alpha \end{bmatrix}$$

with  $r$  the correlation between orthogonal phase forcings and  $\alpha$  the ratio of the forcing variances while  $c$  is the overall strength of the forcing. The correlation between the phases may be non-zero if there is large scale coherent stochastic forcing with a pattern different than the normal mode phases.

In this paper the consistency of the model just described is tested by comparing the power spectrum it produces for the two different ENSO phases with that obtained from observational data sets. The power spectra of the various phases of the model given in Eq. (1) can be obtained analytically. In particular one can derive an expression for the so-called spectral matrix of the problem from which the power spectrum of various phases can then be deduced (Gardiner 2004). These spectra can be productively written in terms of the ENSO phase under consideration, the covariance matrix  $\mathbf{R}$  parameters  $\alpha$ ,  $r$  and  $c$  as well as the system dynamical matrix  $\mathbf{A}$  parameters  $\varepsilon$  and  $\eta$ . A full derivation and detailed discussion may be found in Kleeman (2011). For a general phase vector  $[a, b]^T$  [(i.e. a general linear combination of the standard basis vectors in Eq. (1))] the analytical spectrum is given by

$$S(\omega) = \frac{c(1 + \alpha)(a^2 + b^2)}{8\pi} \times [S_+(\omega) + S_-(\omega) + 2f_{12} \cos(\theta(\omega) + \gamma) \sqrt{S_+(\omega)S_-(\omega)}] \tag{3}$$

Here  $S_{\pm}(\omega)$  are the broadband symmetric Lorentzian functions:

$$S_{\pm}(\omega) = \frac{1}{\varepsilon^2 + (\omega \pm \eta)^2}. \tag{4}$$

They are centered on plus or minus the oscillator (or normal mode) frequency  $\eta$  and their spread varies directly with the damping parameter  $\varepsilon$ .

The third and final term in brackets is commonly referred to as the cross-spectrum. This term is a function of  $\gamma$  which is given by

$$\gamma = 2\phi + \delta(r, \alpha) \tag{5}$$

where the offset angle  $\delta$  depends only on the stochastic forcing parameters and  $\phi$  is the phase angle under consideration i.e. we have

$$\cos \phi = \frac{a}{\sqrt{a^2 + b^2}} \tag{6}$$

Note that this means that the cross-spectra of variables that have a phase difference of  $\frac{\pi}{2}$ , such as ENSO and its precursor, have opposite signs. This is the reason why these

two series can have different spectra and, in particular the precursor, can have more decadal weight. This follows because the cross-spectrum has most weight at frequencies less than the oscillator frequency. The other angle  $\theta(\omega)$  is a function of the dynamical parameters  $\omega$ ,  $\eta$  and  $\varepsilon$  only. The Wiener coherence  $f_{12}$  depends on stochastic forcing parameters via the equation:

$$f_{12} = \frac{\sqrt{(1-\alpha)^2 + 4r^2\alpha}}{1+\alpha} \quad (7)$$

The Wiener coherence  $f_{12}$  is a constant in this linear case and equal to the magnitude of the correlation of the normal mode stochastic forcings.

Finally, note that apart from the cosine and Wiener coherence factors, the cross-spectrum is twice the geometric mean of the two diagonal spectra. It follows therefore that the contribution of this term to the total spectrum is controlled by the Wiener coherence. Values of this coefficient of order 0.5 or so will mean that the cross-spectrum becomes an important player in the total spectrum of at least some phases. In the case  $f_{12} = 0$  the cross-spectrum has no contribution to the spectrum and so

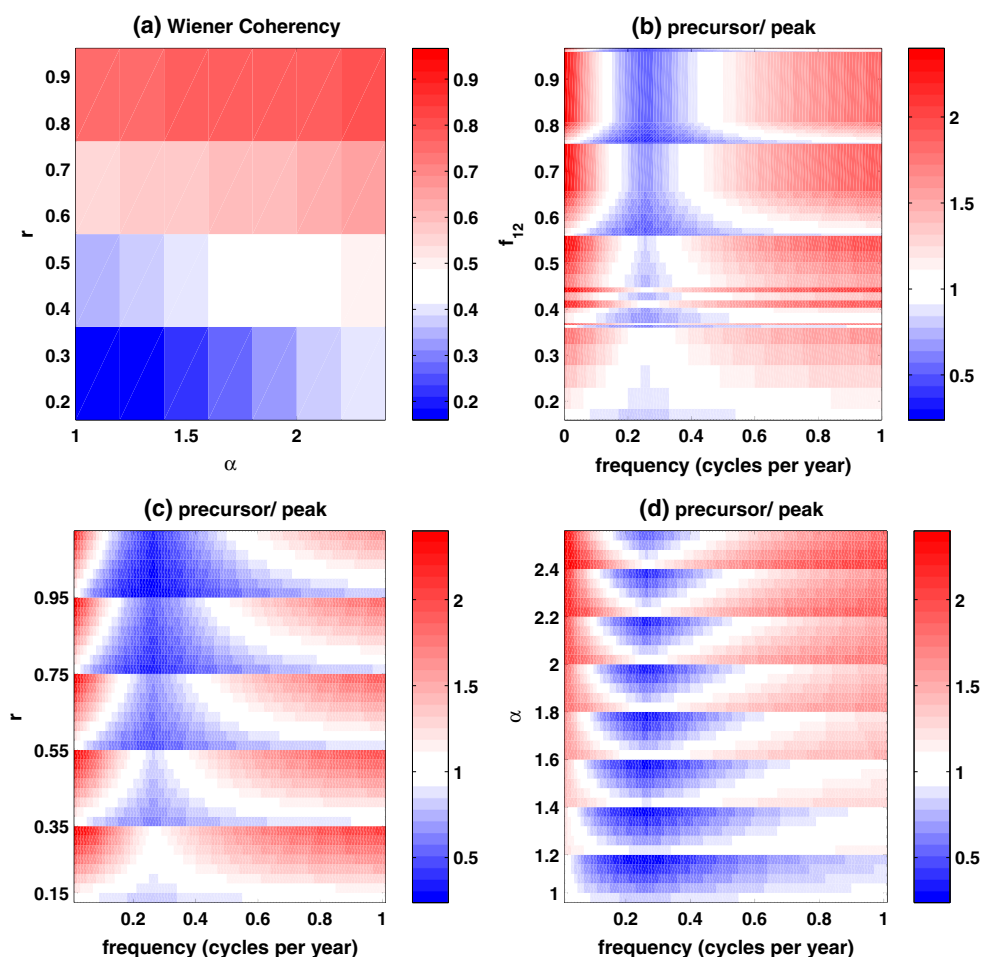
changing the phase angle does not affect the spectrum. On the other hand, for large cross-spectral weight  $f_{12} = 1$  the spectrum changes shape dramatically with phase angle.

The advantage of Eq. (3) is that the spectrum under consideration can be directly related to the various physically significant parameters for the theoretical model. In the following section we use the observational spectra to obtain a best fit estimate for these parameters after looking in some more detail at the relationship of the Wiener coherence and the spectral shape and changes of the spectrum when using a higher dimensional model.

#### 4.2 Relationship of Wiener coherence and spectral shape

To better understand the effect the cross-spectral term in Eq. (3) has on the low frequency part of the spectrum Fig. 9 shows the change in the ratio of precursor to peak spectrum for combinations of  $r$  and  $\alpha$ . Relevant values for  $r$  and  $\alpha$  are chosen based on the fit results in Table 1. The Wiener coherence  $f_{12}$  attains values between 0 and 1 and increases with both  $r$  and  $\alpha$ . For a given  $r$ , Fig. 9c shows that the low

**Fig. 9** Cross spectrum dependence of theoretical peak and precursor spectrum for different forcing statistics. **a** Wiener coherence  $f_{12}$ , which sets the cross-spectral contribution, as a function of the correlation between the phase forcings,  $r$ , and the ratio of the variance of the phase forcings,  $\alpha$ . Ratio of precursor to peak spectrum **b** as a function of the Wiener coherence  $f_{12}$ , **c** as a function of  $r$ , where for each value of  $r$   $\alpha$  increases, and **d** as a function of  $\alpha$ , where for each value of  $\alpha$   $r$  increases



frequency contribution of the precursor increases with increasing  $\alpha$ . On the other hand Fig. 9d shows that for a given  $\alpha$  the low frequency contribution of the precursor decreases with increasing  $r$ . In general the low frequency contribution of the precursor depends strongly on the value of  $\alpha$  and to a lesser degree on the value of  $r$ , which means the low frequency behavior of  $f_{12}$  and the cross-spectrum depends more strongly on  $\alpha$  than on  $r$ .

Recall, that  $f_{12}$  governs the potential strength of the cross-spectral term. If  $f_{12}$  is small then the cross-spectrum is small, if  $f_{12}$  is large the cross-spectrum can be large. The actual size of the cross-spectrum, however, depends not only on  $f_{12}$ , but also on the phase angle  $\gamma$  with depends on the forcing statistics. It is the product of  $f_{12}$  and  $\cos(\theta(\omega) + \gamma)$  that sets the cross-spectrum. Even if  $f_{12}$  is large, but  $\cos(\theta(\omega) + \gamma)$  is small the cross-spectrum will be small.

### 4.3 Higher dimensions

It is conceivable that the observed POP 1 power spectra are influenced by the higher order modes in the ENSO system. What is the influence of higher modes on the dominant mode spectra in the POP model? The theoretical spectrum, when expanding the model to 2 complex modes, can be written as a sum of three terms (see Eq. (11) in appendix). The first two terms are the spectra of the two normal modes respectively, as given in Eq. (3) and the third term represents the addition to the cross-spectrum due to correlations between the forcing onto the normal modes. This third term only becomes important if the decay time ( $\varepsilon_2$ ) of the second mode is sufficiently longer than the decay time ( $\varepsilon_1$ ) of the first mode, the changes of the first mode spectrum by the second mode are most influential close to the second mode period ( $\eta_2$ ).

Figure 10 shows the change in the first mode spectrum by the second mode for two different periods  $\eta_2$  and decay times  $\varepsilon_2$ . The period of the first mode is set to  $\eta_1 = 4$  years and the decay time  $\varepsilon_1 = -9$  months. These values are based on the results presented in Sect. 5. Differences between the mode 1 spectrum and the combined spectrum are largest if the difference between periods is large and also if mode 2 has a much longer decay time than mode 1. Changes do not affect both phases to the same amount, especially near  $\eta_2$ . However, near  $\eta_1$  the shape and strength of the mode 1 spectrum does not change very much even with unrealistically long decay time  $\varepsilon_2$  for mode 2. It is likely that the dominant modes identified by POP analysis have some contribution from other modes in the system. The way the theoretical POP spectra change with addition of more modes makes it clear that the second mode would need to have a very long decay time to alter the mode 1 spectrum significantly. The changes of the theoretical spectra are within the CIs about the observed power

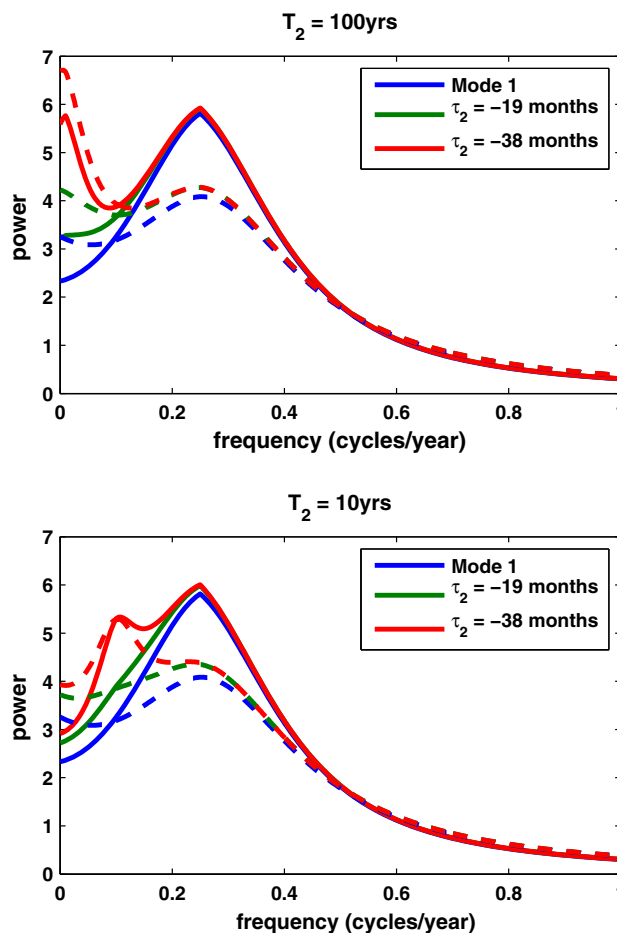


**Fig. 10** Theoretical spectra of both phases of mode 1 for a 2 mode model and the influence of the decay time  $\varepsilon_2$  and period  $\eta$  of the second mode onto the mode 1 spectra. Period  $\eta_1$  and decay time  $\varepsilon_1$  of mode 1 are 4 years and  $-9$  months respectively. Shown are mode 1 phases (blue), both modes with  $\varepsilon_2 = -19$  months (green) and both modes with  $\varepsilon_2 = -38$  months (red). Solid lines are phase 1 spectra dashed lines are phase 2, the phases for both modes are  $90^\circ$  out of phase

spectra. Changes in the observed spectra as can be expected from the theoretical spectrum, are unlikely to change the results of the model parameter estimates presented in the next section.

## 5 Empirical model parameters

### 5.1 Fitting algorithm

Consideration of Eq. (3) shows that to fit the model to observations the parameters to estimate are the phase angle  $\phi$ , the forcing statistics  $\alpha$ ,  $r$ ,  $c$ , and the period and decay parameters  $\eta$  and  $\varepsilon$ . The phase difference between the two time series is fixed to be  $\frac{\pi}{2}$  and the angle of the mature phase is determined from the fit. This assumption is based

on the fact that the lag correlations in Fig. 4 are fairly symmetric about the zero lag which hints at a quadrature behavior between the precursor and mature phase time series on interannual time scales (see also Sect. 6). The parameter values are then estimated by fitting the theoretical spectrum to the observed power spectral curves using nonlinear least-squares. The optimal parameter values minimize a cost function of the sum of squared errors between the theoretical spectrum and the observations. Because the results of the spectral fit depend on the chosen initial conditions 10,000 randomly chosen initial conditions are fitted and the best initial conditions are chosen based on the goodness of fit of the fitted curve and the size of the parameter CIs.

For simplicity, first consider the case where the cross-spectrum is zero. In that case only period and decay time ( $\eta$  and  $\varepsilon$ ) and the overall strength of the stochastic forcing  $c$  need to be estimated. Theoretically this case arises when the forcing projects evenly onto both phases and there is no correlation between the forcings (i.e.  $\alpha = 1$  and  $r = 0$ , compare to Eq. (7)). Fitting the theoretical spectrum in this case (Fig. 11a) with just the peak ENSO phase time series gives a very good fit and estimates the period as 4.1 years and the decay time at 9.8 months. Estimates for CIs at the 95 % level are [3.6, 4.9] years and [7.1, 15.9] months for period and decay time respectively. The value estimated for the period of ENSO is unsurprisingly very close to what has been previously calculated by many authors. The decay time has received less attention but is important from a predictability viewpoint. It corresponds qualitatively well with the practical limit of skillful ENSO predictions of many operational coupled (and statistical) forecast models (Barnston and Ropelewski 1992; Chen and Cane 2008; Izumo et al. 2010). Note that this estimate derives from the spread of the spectrum and is thus fairly tightly constrained by the observations. See Sect. 6 for details on the relation between the short data record, the spectral peak width and the decay time.

Fitting now both the Niño3 and  $z_i^{\text{slp}}$  or  $z_i^{\text{sst}}$  spectra simultaneously, estimates for the forcing parameters are obtained. The additional information contained in the precursor is sufficient to constrain the forcing parameters. The estimated parameter values for several cases, one using Niño3 and the other using SOI as the peak phase, are shown in Table 1. The observed and fitted spectra for the Niño3—20CRSLP case are shown in Fig. 11b. The decay time estimated from the fit is 8 months with CI [7.5, 8.2] months and the period is 4.4 years with CI [4.4, 4.6] years. The fit for the Niño3 spectrum is very similar to the one without the cross-spectral terms, and the overall shape of the precursor and difference with the peak spectrum is captured, however the  $z_i^{\text{slp}}$  spectrum is not as well approximated by the fitted curve.

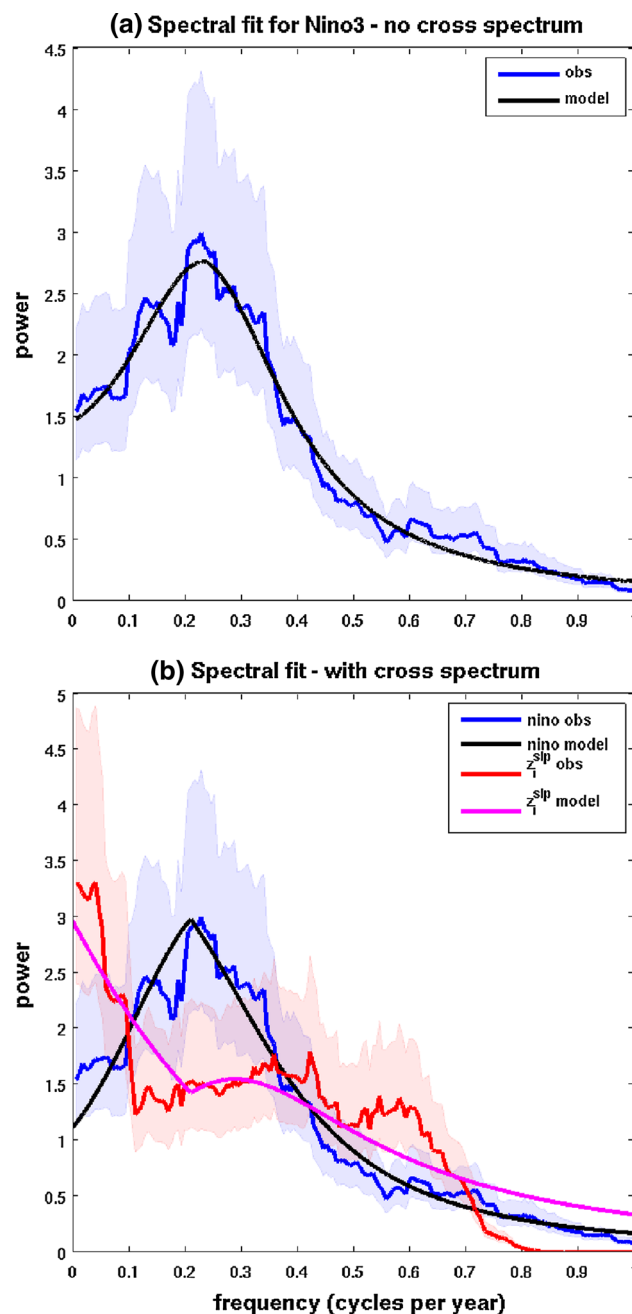


**Fig. 11** Spectral fit to observed power spectra. **a** Niño3 spectrum only, no cross-spectrum. **b** Niño3 and 20CRSLP spectral fit with cross-spectrum. *Shading* are the 90 % CIs around the observed spectra. *Theoretical curves* are fitted using a nonlinear least squares fitting algorithm

For all considered data sets the stochastic forcing estimated has a variance ratio  $\alpha$  significantly larger than 1 i.e. greater variance for the peak rather than precursor phase (see below). The correlation between the two forcings is  $r = 0.5 - 0.7$  for SLP precursors and  $r = -1$  for SST precursors, which does not appear unreasonable. These two values imply that the Wiener coherency is  $f_{12} \geq 0.5$  for all

**Table 1** List of the parameter values and confidence intervals obtained from spectral fit for Niño3 and SOI mature phase data and SLP and SST POP time series for the precursor

	Niño3-SLPhad2	Confidence interval	Niño3-SLPerslp	Confidence interval	Niño3-20CRSLP	Confidence interval
$\alpha$	2.09	(1.88, 2.29)	1.5	(1.35, 1.65)	2.17	(1.87, 2.48)
$c$	0.45	(0.41, 0.49)	1.07	(0.76, 1.38)	0.60	(0.35, 0.86)
$\phi$	3.14	(3.14, 3.14)	-0.55	(-0.63, -0.47)	-0.18	(-0.38, 0.02)
$r$	-0.63	(-0.7, -0.55)	-0.62	(-0.71, -0.53)	-0.72	(-0.84, -0.61)
$\varepsilon$	<b>-7.99</b>	(-8.24, -7.47)	<b>-6.97</b>	(-7.66, -6.40)	<b>-7.00</b>	(-7.55, -6.53)
$\eta$	<b>4.41</b>	(4.40, 4.63)	<b>4.50</b>	(4.28, 4.74)	<b>4.77</b>	(4.55, 5.02)
	SOI SLPhad2	Confidence interval	SOI - LPerslp	Confidence interval	SOI - 20CRSLP	Confidence interval
$\alpha$	2.05	(1.91, 2.19)	1.73	(1.59, 1.88)	2.24	(2.09, 2.40)
$c$	0.81	(0.58, 1.05)	1.65	(1.25, 2.06)	0.96	(0.65, 1.27)
$\phi$	-0.29	(-0.47, -0.12)	-0.61	(-0.66, -0.57)	-0.34	(-0.49, -0.20)
$r$	0.57	(0.53, 0.62)	-0.72	(-0.78, -0.67)	0.71	(0.67, 0.76)
$\varepsilon$	<b>-7.47</b>	(-7.96, -7.03)	<b>-6.47</b>	(-6.98, -6.04)	<b>-6.69</b>	(-7.17, -6.27)
$\eta$	<b>4.34</b>	(4.17, 4.52)	<b>4.48</b>	(4.30, 4.67)	<b>4.63</b>	(4.43, 4.85)
	Niño3-SSThad3	Confidence interval	Niño3-SSTersst3b	Confidence interval	Niño3-SSThadisst	Confidence interval
$\alpha$	2.76	(2.46, 3.06)	3.03	(2.61, 3.45)	2.72	(2.49, 2.94)
$c$	0.71	(0.43, 0.99)	0.63	(0.34, 0.93)	0.47	(0.34, 0.59)
$\phi$	-0.20	(-0.30, -0.11)	-0.23	(-0.33, -0.13)	-0.08	(-0.16, -0.01)
$r$	-1.0	(-1.0, -1.0)	-1.0	(-1.0, -1.0)	-1.0	(-1.0, -1.0)
$\varepsilon$	<b>-6.61</b>	(-7.60, -6.01)	<b>-6.92</b>	(-7.97, -6.04)	<b>-7.07</b>	(-7.83, -6.44)
$\eta$	<b>5.59</b>	(5.07, 5.83)	<b>6.03</b>	(5.55, 6.61)	<b>5.37</b>	(5.07, 5.70)

Note that the values for decay time and period are given in bold and the units are months and years respectively. Confidence intervals are at the 95 % level

cases, which means that the cross-spectrum has a significant amplitude. This is consistent with the spectra for the two phases having significant qualitative differences at low frequencies.

### 5.2 Model with estimated parameters

To test the validity of the simple model the estimated parameter values are used to numerically generate time series with the theoretical model. The model stochastic forcing is extracted from the covariance structure of the forcing using standard linear algebra methods (see “Appendix 3” for details). A sufficiently long time series is generated to ensure the process reaches (statistical) equilibrium and consequently its spectrum approaches the equilibrium spectrum.

The relationship between the modeled time series  $x, y$  and their spectra, and the original peak and precursor time series is determined through the fitted phase angle. Denoting the modeled mature phase by  $z_r$  and the modeled precursor phase by  $z_i$ . The mature phase is associated with phase angle  $\phi$  and the precursor phase therefore with  $\psi = \phi + \frac{\pi}{2}$ . Mature and precursor phases are recovered as linear combinations of

$x$  and  $y$ , with the coefficients determined by the phase angles. Details of this and the linear transformation mapping  $(x, y)$  to  $(z_r, z_i)$  (the mature phase – precursor phase basis) can be found in “Appendix 4”.

The spectra of a realization of the modeled stochastic process match the observed spectra reasonably well (not shown). The modeled peak spectrum has its peak at approximately the right frequency although the peak is leaner and somewhat larger than in the observed Niño3 spectrum. The  $z_i$  spectrum has less power than  $z_r$  at all but the lowest frequencies, where  $z_i$  dominates over  $z_r$ . The main differences between data and model spectra are a smaller increase in power for the low frequencies in the  $z_i$  spectrum and more power in the  $z_i$  spectrum for ENSO frequencies compared to observations. The lag correlation between mature and precursor phases are very similar to the data correlations in Fig. 4, both in strength and location of maximum correlation at approximately 7 months. There is a slight asymmetry between the leading and following peak also consistent with observations.

Using the values for the parameters given in Table 1 we can estimate the variances and correlation of the forcing that generates the  $z_r$  and  $z_i$  time series (see “Appendix 3”

for details on how the covariance matrix for  $(z_r, z_i)$  is derived). For the two spectra given in Fig. 11 (i.e. the parameters from the Niño3-20CrSLP fit) the correlation matrix for the forcing is

$$\tilde{\mathbf{R}} = 1.5 \begin{bmatrix} 1 & -0.31 \\ -0.31 & 0.27 \end{bmatrix}. \quad (8)$$

where the covariance matrix is normalized so that the variance of the forcing onto the  $z_r$  component is unity. Equation 8 shows that the variance of the forcing onto the precursor component  $z_i$  is only about 30 % of the forcing onto the peak phase. Other data combinations for the fit give similar results; with weaker forcing on the precursor phase of ENSO than on the mature phase. The correlations between the forcing onto precursor and peak phase are not negligible, as expected from observations.

The difference in forcing variance onto the two phases is an interesting result, because it implies weaker forcing of the ENSO signal in the western rather than in the eastern equatorial Pacific (the main loading regions of the precursor and peak patterns respectively). This is a plausible result, considering that the western Pacific warm pool region has the highest SSTs in the world. Therefore small SST anomalies will be enhanced by the large background SSTs in that region. The atmosphere, and convection in particular, responds to absolute values of SST rather than the anomalies. SST anomalies in the western Pacific can therefore induce a disproportionately larger atmospheric response compared to the same anomalies in the eastern tropical Pacific. It is also interesting to note that this difference in stochastic forcing could theoretically be verified from observational data. This is beyond the scope of this study, but provides a testing and verification mechanism for the model and parameter values proposed here.

## 6 Discussion

In this paper observed SST and SLP POP power spectra are used to estimate model parameters for a two-dimensional stochastically forced damped linear oscillator. One of the main results of the diagnostic presented here is the estimation of mean period and decay time of the ENSO oscillation. The estimated decay time of 8 months is close to the practical ENSO prediction limit (Barnston and Ropelewski 1992; Chen and Cane 2008; Izumo et al. 2010). Due to the short climate record there is some uncertainty in the observed power spectra and the width of the spectral peak which is directly related to the model decay time. Is our estimate of the decay time an underestimate or overestimate? Uncertainty in the period due to a short data record results in a broadening of the observed spectral peak compared to the actual spectrum. A broader peak translates to a

shorter decorrelation time of the underlying phenomenon. So the uncertainty in the climate record makes it more likely we underestimate the decay time of the oscillation. Using power spectra to estimate the decay time of the oscillation is advantageous over using the decay time obtained from the POP analysis in that the eigenvalues that the POP decay time relies on depend strongly on the spatial domain. The power spectra are found not to be very sensitive to changes in the spatial domain.

The issue of non-normality of the ENSO system has not been addressed so far. The simple model and diagnostic based on only one normal mode, the first POP, presented here, yields good results for the estimation of decay time and mean period of the ENSO system. However, it has been argued that ENSO may be significantly non-normal and that multiple normal modes are necessary to accurately describe instability growth in the system (Penland and Sardeshmukh 1995; Moore and Kleeman 1998). The results presented here indicate that non-normality may be less important for the long-term spectrum. An extension of the simple model and analysis that includes the second POP would be instructive, as this would introduce non-normality into the model, the two modes not being orthogonal, but is outside the scope of this current work.

That the POP model should be able to reproduce the observed decadal variability in the Pacific is not obvious. A POP analysis assumes an underlying linear system where the system matrix is estimated from the data and the decaying oscillation is subjected to stochastic forcing. For the leading POP mode that describes ENSO variability the system reduces to two dimensions. Theoretically, if the random forcing of the two components (real and imaginary part of the complex POP mode) is assumed to have some small correlation then the spectrum of one of the components shows significantly more weight for periods longer than the peak ENSO period. It is feasible that such small correlations between the forcing of both modes of the ENSO cycle exist: The random forcings arise from atmospheric transients which have a large scale horizontal structure. This implies that there should be some spatial overlap in the structure of the two random forcings, leading to a small correlation of the two forcing pattern time series.

Consider a reconstruction of the data using only the first POP mode  $X = z_r(t)P_r(x, y) + z_i(t)P_i(x, y)$ . Time filtering of this reconstruction affects only the POP coefficients and not the spatial patterns. That means that on decadal and interannual time scales the reconstruction is based on the same patterns, but the time series multiplying these patterns are different. In particular the decadal and interannual parts of the POP coefficients have very different spectral characteristics (Fig. 12) and so the dominant patterns will differ. The decadal part of the POP is defined as in Sect. 3.4, and the interannual part as the difference between the

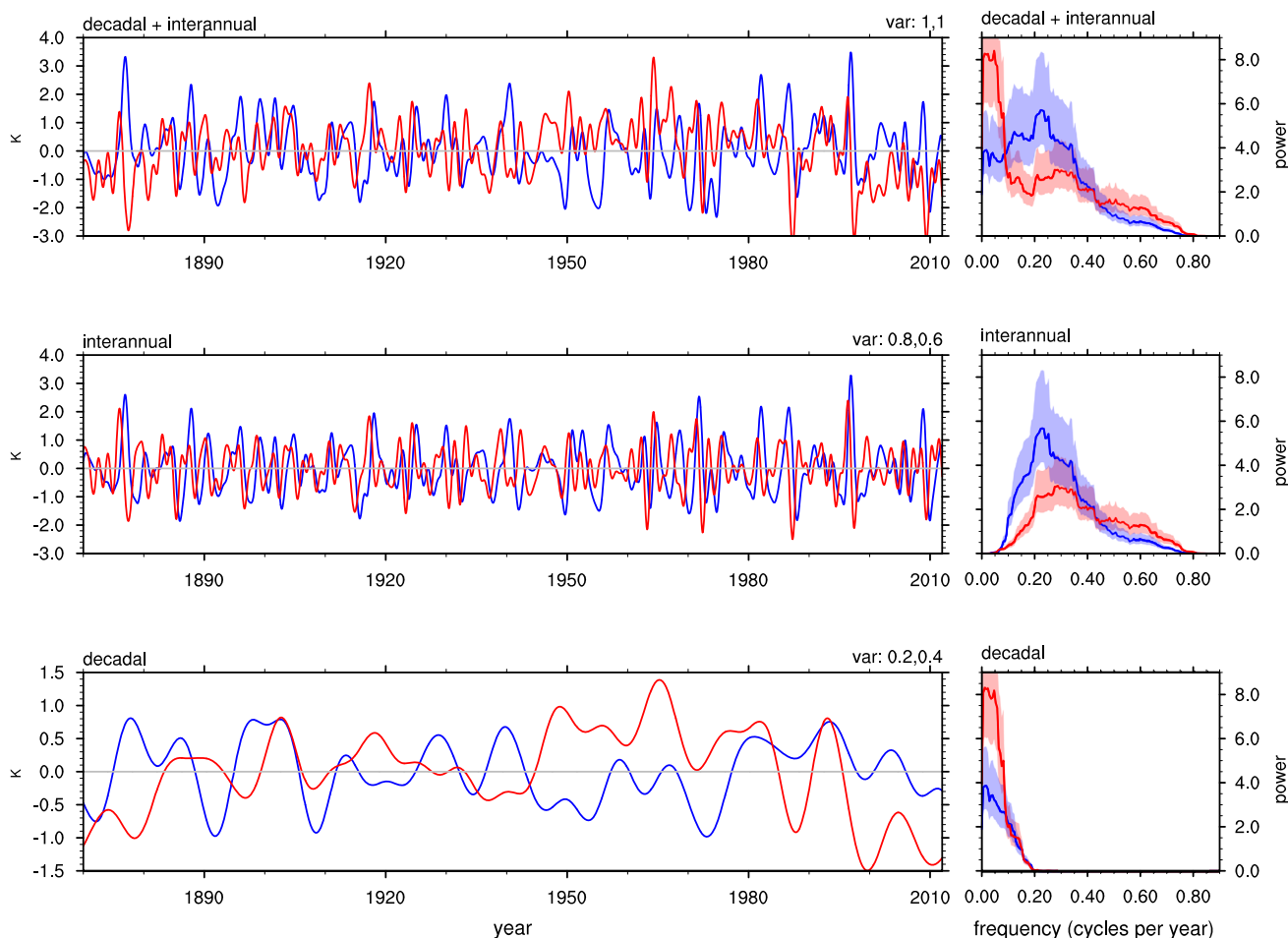


**Fig. 12** HadISST POP 1 time series and spectra for decadal and interannual time scales. Peak ENSO phase is shown in *blue* and the precursor in *red*. Decadal time scales are obtained by low-pass filtering the POP time series using a 193 point (16 year) low-pass Lanczos filter with a half-power point at 0.12 or 8.3 years. The interannual part is the difference between the original time series and the decadal part. *Above each panel* the variance for the peak (*left*)

and precursor (*right*) are noted. The interannual part has a larger variance for both peak and precursor, but the precursor dominates over the peak in terms of variance for decadal time scales whereas the peak phase has more variance than the precursor at interannual time scales. The panels on the right show the corresponding power spectra for peak and precursor filtered for the different time scales. As before, shading are the 90 % confidence intervals around the observed spectra

original POP time series and the decadal part. This linear decomposition assumes that both time scales vary independently and the decadal part modulates the interannual. The assumption is consistent with the fact that variations on decadal time scales are much smaller than on interannual time scales. When POP time series are normalized to have variance 1 (both peak and precursor), then for the HadISST POP time series variance on interannual time scales is 0.8 and 0.6, on decadal time scales 0.2 and 0.4, for peak and precursor respectively. The interannual part is more consistent with the quadrature relation between peak and precursor (Fig. 12, middle panels). The maximum correlation 8 months prior to El Niño events increases from 0.5 for the interannual plus decadal part to 0.7 for the interannual part only of the POP coefficients.

The POP analysis identifies one possible precursor for ENSO. This does not mean that this is the only possible precursor. The spectral power at ENSO frequencies in the precursor is significantly lower than for the peak phase. This indicates that other processes can lead to El Niño events than described by the precursor. Output from long control runs of two CMIP5 models has been used to assess the potential variability of the POP spectra on longer time scales. The control runs were split into several 150 year segments and SST and SLP POPs for each segment are computed as for the observations. There are considerable differences among the precursor spectra for different segments, while the variability in the peak spectra is noticeably less. This large variability in the precursor suggests several issues, that we highlight below:

- The possibility that the models do not adequately replicate the real world.
- That during the different periods the forcing statistics change. When both (peak and precursor) spectra are similar to observations the forcing variance onto both phases is different and the forcings are correlated. When both spectra are identical there is no correlation between the phase forcings and the variance of the forcing is the same.
- Different mechanisms of ENSO development may be dominant during different periods.

Consistent with this last hypothesis (although on shorter time scales) is the fact that 20 year windowed correlations between the peak and precursor time series varies over the length of the record (Fig. 4). The correlation between Niño indices and SST precursors, which can also be used as a proxy for the correlation between peak and precursor (as the correlation between the peak and Niño indices is about 0.9 at zero lag) was around 0.6 prior to 1930 and after 1960, and much lower between these dates. Some of this may be due to data issues going back in time or the low ENSO variability during that time interval, but evidence points to the latter being dominant (Trenberth 1976).

It is feasible to apply the diagnostic methods used here to long climate model runs from models able to reproduce ENSO variability and this complex mode oscillation. A comparison of the spectra, and through those of the forcing statistics, with the control run spectra and observations, can be used to shed light on changes in the importance of the precursor identified by the POP analysis in a changing climate.

The diagnostic methods used here are applicable to other physical phenomena, provided it is appropriate to approximate these phenomena by a linear stochastic system. The simple model can be extended to include multiple normal modes as indicated by the 2 mode spectrum analyzed in Sect. 4.3. Currently under investigation is the application to Convectively Coupled Equatorial Waves (CCEWs) and the Madden-Julian Oscillation. Observational and modeling evidence (Wheeler and Kiladis 1999; Yang et al. 2007; Dias and Pauluis 2009; Gehne and Kleeman 2012) suggests that these can be modeled using linear shallow water equations with a reduced phase speed due to convection. Including additive white noise forcing leads to the spread of power around the theoretical linear shallow water dispersion lines as seen in observations.

## 7 Summary

In this paper a two-dimensional stochastically forced damped linear oscillator model is proposed as a useful diagnostic for estimating the decay time, mean period and

forcing statistics of ENSO. Model parameters are estimated from a POP analysis which identifies a complex oscillatory mode of the climate system. The leading mode diagnosed by the POP analysis is a physically relevant mode of the climate system identified with ENSO. The real part of the mode projects strongly onto the leading EOF, which explains a large amount of the variance of the oscillatory mode of the coupled ocean-atmosphere system. The imaginary part of the oscillatory mode is a precursor to the peak with negative SST anomalies in the western Pacific and low pressure nodes in the central off-equatorial Pacific in both hemispheres. We use the analytical solutions for spectral properties of multi-dimensional geophysical models found by Kleeman (2011) to fit the observed power spectra of peak and precursor phase, thereby identifying model parameters of a two dimensional stochastically forced damped linear oscillator. The theoretical spectrum and model allow us to reproduce the observed behavior of the power spectra and interpret their shape in terms of the decay time and forcing statistics of the simple model.

We show here that the estimated stochastic forcings onto the two phases are correlated and the variance of the forcing on the precursor is smaller than that on the peak ENSO phase. This is due to the fact that for observed ENSO phases the peak dominates at interannual frequencies while the precursor dominates at decadal frequencies. The conclusion from the reversal in maximum power for decadal frequencies in the phase spectra follows: if one low-pass filters the data for decadal frequencies then one component of the ENSO cycle will be more emphasized over the other compared to an analysis that includes both decadal and interannual time scales. Variations on decadal time scales are much smaller than on interannual time scales, indicating that the decadal part acts similarly to a modulation of the interannual part. The linear decomposition of the time series means that on decadal and interannual time scales POP 1 is based on the same patterns, but the decadal and interannual parts of the POP coefficients have very different spectral characteristics. Thus the ENSO precursor having a spectrum with greater decadal weight than the peak ENSO pattern could at least partly explain why the decadal signal in the Pacific looks different from the interannual.

In addition we obtain a robust estimate of the decay time of the ENSO oscillator, as described by the leading POP pair, of about 8 months. Several different SST and SLP data sets are used to verify this value and all give consistent results. Shorter than some previous estimates of the decay time of ENSO, this value corresponds to the practical ENSO prediction limit.

The appearance of the precursor signal in SST as well as SLP is examined. The spatial patterns of SST and SLP precursor are shown to be dynamically consistent and we

give a physical interpretation for the relationship between the precursors for these two variables. The location of the low pressure systems in the SLP precursor to the east of anomalous low precursor SSTs in the western equatorial Pacific is consistent with cooling of the mixed layer in that region during the onset of El Niño. This cooling in SST shifts the warmest ocean temperatures eastward and with that the region of most vigorous convection, leading to the development of anomalous low pressure systems in the central Pacific. In the context of the simple model, atmospheric transients act as stochastic forcing on SST anomalies which are related to dynamical changes in ocean heat content. Ocean heat content changes on slower time scales than the atmosphere and provides memory to the oscillation. The oscillation in SST then leads to a response in large scale SLP. The atmospheric component thus provides the stochastic forcing, but also responds to the SST dynamics.

**Acknowledgments** We would like to thank two anonymous reviewers for their constructive comments, helping to improve this manuscript. We would like to acknowledge that the NOAA ERS-STv3, Extended Reconstructed SLP, HadSLP2 and 20CrSLP data were provided by the NOAA/OAR/ESRL PSD, Boulder, Colorado, USA, from their Web site at <http://www.esrl.noaa.gov/psd>. The HadSST3 and HadISST data was provided by the UK Met Office at <http://www.metoffice.gov.uk/hadobs/>. The Niño indices and SOI data were provided by the IRI/LDEO Climate Data Library and are available from their Web site at <http://iridl.ldeo.columbia.edu>. Gehne and Kleeman also acknowledge the support of the NSF grant ATM0806721. Gehne and Trenberth acknowledge the support of the NASA grant X11AG69G.

## Appendix

### 1 Additional data sets

In addition to the data sets presented in this study the analyses described above were applied to the following data sets as well. The extensively documented Hadley Centre global SLP data version 2 (HadSLP) is available at 5° resolution from January 1850 to December 2004 (Allan and Ansell 2006). NOAA reconstructed sea surface temperature data version 3b (ERSST) available on a 2° grid from January 1854 to February 2011 (Smith et al. 2008). For comparison the Hadley Centre global 5° SST anomaly data version 3 (HadSST) (Kennedy et al. 2011a, b), available from January 1850 to December 2007, and the NOAA extended reconstructed 2° SLP (ERSLP) data set (Smith and Reynolds 2004) available from January 1854 to December 1997 were also used.

Results obtained using these data sets are consistent with those from HadISST and 20CrSLP. The POP patterns for the first pair are almost identical with only small

differences. The time series for the peak phase are highly correlated between the data sets and with Niño3. Correlations for the precursors are lower and show higher variability (Fig. 4). The POP power spectra for different data sets and variables have similar characteristics (Fig. 5) and the fitted parameter values agree well (Table 1).

### 2 Theoretical spectrum for 2 modes

The theoretical spectrum for a 2 mode model is computed to analyze how the inclusion of more than one mode in the theoretical model influences the power spectra for the first mode. Analogous to the damped harmonic oscillator with stochastic forcing described in Sect. 4 we can compute the spectrum for a 2 mode oscillation:

$$d \begin{bmatrix} x_1 \\ y_1 \\ x_2 \\ y_2 \end{bmatrix} = \mathbf{A} \begin{bmatrix} x_1 \\ y_1 \\ x_2 \\ y_2 \end{bmatrix} dt + \mathbf{F}dW, \tag{9}$$

where

$$\mathbf{A} = \begin{bmatrix} \varepsilon_1 & -\eta_1 & 0 & 0 \\ \eta_2 & \varepsilon_2 & 0 & 0 \\ 0 & 0 & \varepsilon_2 & -\eta_2 \\ 0 & 0 & \eta_2 & \varepsilon_2 \end{bmatrix} \tag{10}$$

with  $\mathbf{F}$  the (4D) forcing matrix and  $W$  the (vector) Wiener stochastic process.

The stochastic forcing in Eq. (9) has an associated covariance matrix  $\mathbf{R}$ . This contains as parameters the variance of the forcing on the four phases as well as the correlation between them. It can be written as

$$\mathbf{R} = \mathbf{F}\mathbf{F}^T = c_1 \begin{bmatrix} 1 & r_{12}\sqrt{\alpha_2} & r_{13}\sqrt{\alpha_3} & r_{14}\sqrt{\alpha_4} \\ r_{12}\sqrt{\alpha_2} & \alpha_2 & r_{23}\sqrt{\alpha_2\alpha_3} & r_{24}\sqrt{\alpha_2\alpha_4} \\ r_{13}\sqrt{\alpha_3} & r_{23}\sqrt{\alpha_2\alpha_3} & \alpha_3 & r_{34}\sqrt{\alpha_3\alpha_4} \\ r_{14}\sqrt{\alpha_4} & r_{24}\sqrt{\alpha_2\alpha_4} & r_{34}\sqrt{\alpha_3\alpha_4} & \alpha_4 \end{bmatrix}$$

where  $\alpha_i = c_i/c_1$  is the ratio of the variance of phase  $i$  and phase 1.

For a general phase vector  $v = [A, B, C, D]$  the spectrum is:

$$S_v = vS(\omega)v^* = \frac{c_1}{8\pi} [S_v^1(\omega) + S_v^2(\omega) + S_v^{12}(\omega)] \tag{11}$$

with the first 2 terms equal to the spectra for each mode

$$S_v^1(\omega) = (1 + \alpha_2)(A^2 + B^2) [S_+^1(\omega) + S_-^1(\omega) + 2f_{12} \cos(\gamma_{AB} + \arccos(\varepsilon_1 S_-^1(\omega)) - \arccos(\varepsilon_1 S_+^1(\omega))) \sqrt{S_+^1(\omega)S_-^1(\omega)}] \tag{12}$$

and similarly for the second mode spectrum  $S_v^2(\omega)$ . The third term in Eq. (11) is the spectral contribution due to the correlation between the mode forcings. This can be written as

$$S_v^{12}(\omega) = 2\sqrt{(A^2 + B^2)(C^2 + D^2)} [f_+(X_+^{12} + X_-^{12}) + f_-(Y_+^{12} + Y_-^{12})] \quad (13)$$

with

$$X_+^{12} = \cos(\phi_+^{12})\sqrt{S_-^1(\omega)S_-^2(\omega)} \quad (14)$$

$$X_-^{12} = \cos(\phi_-^{12})\sqrt{S_+^1(\omega)S_+^2(\omega)} \quad (15)$$

$$Y_+^{12} = \cos(\psi_+^{12})\sqrt{S_-^1(\omega)S_+^2(\omega)} \quad (16)$$

$$Y_-^{12} = \cos(\psi_-^{12})\sqrt{S_+^1(\omega)S_-^2(\omega)} \quad (17)$$

$$f_{\pm} = \sqrt{(r_{13}\sqrt{\alpha_3} \pm r_{24}\sqrt{\alpha_2\alpha_4})^2 + (r_{23}\sqrt{\alpha_2\alpha_3} \mp r_{14}\sqrt{\alpha_4})^2} \quad (18)$$

and

$$\phi_+^{12} = \arctan\left(\frac{BC - AD}{AC + BD}\right) + \arccos\left(\frac{r_{13}\sqrt{\alpha_3} + r_{24}\sqrt{\alpha_2\alpha_4}}{f_+}\right) - \arccos(\varepsilon_1 S_-^1(\omega)) + \arccos(\varepsilon_2 S_-^2(\omega))$$

$$\phi_-^{12} = -\arctan\left(\frac{BC - AD}{AC + BD}\right) + \arccos\left(\frac{r_{13}\sqrt{\alpha_3} + r_{24}\sqrt{\alpha_2\alpha_4}}{f_+}\right) - \arccos(\varepsilon_1 S_+^1(\omega)) + \arccos(\varepsilon_2 S_+^2(\omega))$$

$$\psi_+^{12} = \arctan\left(\frac{BC + AD}{AC - BD}\right) + \arccos\left(\frac{r_{13}\sqrt{\alpha_3} - r_{24}\sqrt{\alpha_2\alpha_4}}{f_-}\right) - \arccos(\varepsilon_1 S_-^1(\omega)) + \arccos(\varepsilon_2 S_+^2(\omega))$$

$$\psi_-^{12} = -\arctan\left(\frac{BC + AD}{AC - BD}\right) + \arccos\left(\frac{r_{13}\sqrt{\alpha_3} - r_{24}\sqrt{\alpha_2\alpha_4}}{f_-}\right) - \arccos(\varepsilon_1 S_+^1(\omega)) + \arccos(\varepsilon_2 S_-^2(\omega)).$$

### 3 Forcing for stochastic model

To generate time series using the theoretical model and the estimated model parameters, it is necessary to get an expression for the stochastic forcing matrix. The covariance matrix  $\mathbf{R}$  of the stochastic forcing is directly given using the

estimated parameters  $c, r$  and  $\alpha$ . The forcing  $\mathbf{F}$  can be obtained from the covariance matrix by computing its eigendecomposition:

$$\mathbf{R} = \mathbf{L}\mathbf{D}\mathbf{L}^{-1}$$

As  $\mathbf{R}$  is a real, positive definite, symmetric matrix  $\mathbf{L}$  is hermitian and satisfies  $\mathbf{L}^{-1} = \mathbf{L}^T$  and all the eigenvalues in  $\mathbf{D}$  are positive. With  $\mathbf{F} = \mathbf{L}\sqrt{\mathbf{D}}$  we define a forcing with the correct covariance matrix since:

$$\mathbf{F}\mathbf{d}\mathbf{B}_t(\mathbf{F}\mathbf{d}\mathbf{B}_t)^T = \mathbf{F}\mathbf{d}\mathbf{B}_t(\mathbf{d}\mathbf{B}_t)^T\mathbf{F}^T = \mathbf{F}\mathbf{F}^T = \mathbf{L}\mathbf{D}\mathbf{L}^{-1} = \mathbf{R},$$

where  $W = [W^1, W^2]^T$  and the  $W^i, i = [1, 2]$  are uncorrelated Wiener processes.

### 4 Peak and precursor phase recovery

We denote the modeled Niño3 time series by  $z_r$  and the modeled precursor phase by  $z_i$ . The phase angles for these time series are  $\phi$  and  $\psi = \phi + \frac{\pi}{2}$  respectively. These phases are related to the theoretical model time series  $x$  and  $y$  in Eq. 1 through linear combinations with coefficients  $\cos\phi$  and  $\sin\phi$  for the mature phase and similarly with phase angle  $\psi$  for the precursor. This means that we can write  $z_r$  and the modeled  $z_i^{\text{slp}}$  or precursor phase time series (denoted by  $z_i$ ) as the following linear combination of  $x$  and  $y$ :

$$\begin{bmatrix} z_r \\ z_i \end{bmatrix} = \begin{bmatrix} \cos(\phi)y + \sin(\phi)x \\ \cos(\psi)y + \sin(\psi)x \end{bmatrix} = \begin{bmatrix} \sin(\phi) & \cos(\phi) \\ \sin(\psi) & \cos(\psi) \end{bmatrix} \begin{bmatrix} x \\ y \end{bmatrix}.$$

Defining

$$\mathbf{Q} = \begin{bmatrix} \sin(\phi) & \cos(\phi) \\ \sin(\psi) & \cos(\psi) \end{bmatrix}$$

this is the linear transformation from the  $(x, y)$  basis to the  $(z_r, z_i)$  basis.

The same linear transformation also transforms the forcing matrix  $\mathbf{F}$ . The forcing covariance matrix in  $(z_r, z_i)$  coordinates is given by  $\tilde{\mathbf{R}} = \mathbf{Q}\mathbf{R}\mathbf{Q}^T$  where the diagonal elements of  $\tilde{\mathbf{R}}$  now give the forcing variances onto  $z_r$  and  $z_i$  and the off-diagonals represent the correlation between the forcings onto  $z_r$  and  $z_i$ . In the case of Niño3 and 20CrSLP results the phase angles are  $\phi = -0.18$  and  $\psi = 1.39$  and the transformation is

$$\mathbf{Q} = \begin{bmatrix} -0.18 & 0.98 \\ 0.98 & 0.18 \end{bmatrix}.$$

The covariance matrix in  $(z_r, z_i)$  coordinates is given by

$$\tilde{\mathbf{R}} = 1.5 \begin{bmatrix} 1 & -0.31 \\ -0.31 & 0.27 \end{bmatrix},$$

where now the (1, 1) entry gives the variance of the forcing onto the peak phase  $z_r$ , and the (2, 2) entry gives the ratio of the forcing variance of the precursor  $z_i$  to the peak. For all considered data sets and both variables this ratio is always less than 1, indicating that the forcing variance on the precursor is smaller than on the peak phase.

## References

- Alexander MA, Blade I, Newman M, Lanzante JR, Lau NC, Scott JD (2002) The atmospheric bridge: the influence of ENSO teleconnections on air-sea interaction over the global oceans. *J Clim* 15:2205–2231
- Allan R, Ansell T (2006) A new globally complete monthly historical gridded mean sea level pressure dataset (HadSLP2): 1850–2004. *J Clim* 19:5816–5842
- Anderson BT (2003) Tropical Pacific sea-surface temperatures and preceding sea level pressure anomalies in the subtropical north Pacific. *J Geophys Res* 108:4732. doi:10.1029/2003JD003805.
- Anderson BT, Furtado JC, Cobb KM, Di Lorenzo E (2013) Extratropical forcing of El Niño–Southern Oscillation asymmetry. *Geophys Res Lett* 40:4916–4921
- Barnett T, Graham N, Cane M, Zebiak S, Dolan S, O’Brien J, Legler D (1988) On the prediction of the El Niño of 1986–1987. *Science* 241:192–196
- Barnston AG, Ropelewski CF (1992) Prediction of ENSO episodes using canonical correlation analysis. *J Clim* 5:1316–1345
- Bjerknes J (1969) Atmospheric teleconnections from the equatorial Pacific. *Mon Weather Rev* 97:163–172
- Burgers G, Jin F-F, van Oldenborgh GJ (2005) The simplest ENSO recharge oscillator. *Geophys Res Lett* 32:L13706. doi:10.1029/2005GL022951
- Cane MA, Zebiak SE (1985) A theory for El Niño and the Southern Oscillation. *Science* 228:1085–1087
- Chang P, Wang B, Li T, Ji L (1994) Interactions between the seasonal cycle and the Southern Oscillation—frequency entrainment and chaos in a coupled ocean-atmosphere model. *Geophys Res Lett* 21:2817–2820
- Chen D, Cane MA (2008) El Niño prediction and predictability. *J Comput Phys* 227(7):3625–3640
- Chen D, Cane MA, Kaplan A, Zebiak SE, Huang D (2004) Predictability of El Niño over the past 148 years. *Nature* 428(6984):733–736
- Compo G, Whitaker J, Sardeshmukh P, Matsui N, Allan R, Yin X, Gleason B, Vose R, Rutledge G, Bessemoulin P, Brnnimann S, Brunet M, Crouthamel R, Grant A, Groisman P, Jones P, Kruk M, Kruger A, Marshall G, Maugeri M, Mok H, Trigo R, Wang X, Woodruff S, Worley S (2011) The twentieth century reanalysis project. *Q J R Meteorol Soc* 137:1–28. doi:10.1002/qj.776.
- Delcroix T, McPhaden M (2002) Interannual sea surface salinity and temperature changes in the western Pacific warm pool during 1992–2000. *J Geophys Res* 107(C12):8002. doi:10.1029/2001JC000862
- Deser C, Wallace JM (1990) Large-scale atmospheric circulation features of warm and cold episodes in the tropical Pacific. *J Clim* 3:1254–1281
- Deser C, Phillips A, Tomas R, Okumura Y, Alexander M, Capotondi A, Scott J, Kwon YO, Ohba M (2012) ENSO and Pacific decadal variability in the Community Climate System Model version 4. *J Clim* 25:2622–2651
- Di Lorenzo E, Cobb KM, Furtado JC, Schneider N, Anderson B, Bracco A, Alexander MA, Vimont DJ (2010) Central Pacific El Niño and decadal climate change in the North Pacific Ocean. *Nature Geosci* 3(11):762–765
- Dias J, Pauluis O (2009) Convectively coupled waves propagating along an equatorial ITCZ. *J Atmos Sci* 66:2237–2255
- Fedorov AV, Harper SL, Philander SG, Winter B, Wittenberg A (2003) How predictable is El Niño? *Bull Am Meteorol Soc* 84(7):911–919
- Folland CK, Renwick JA, Salinger MJ, Mullan AB (2002) Relative influences of the interdecadal Pacific oscillation and ENSO on the South Pacific convergence zone. *Geophys Res Lett* 29(13). doi:10.1029/2001GL014201
- Gardiner CW (2004) *Handbook of stochastic methods*, 3rd edn. Springer, Berlin
- Gehne M, Kleeman R (2012) Spectral analysis of tropical atmospheric dynamical variables using a linear shallow water modal decomposition. *J Atmos Sci* 69:2300–2316
- Harrison D, Vecchi G (2001) El Niño and La Niña—equatorial thermocline depth and sea surface temperature anomalies 1986–1998. *Geophys Res Lett* 28:1051–1054
- Izumo T, Vialard J, Lengaigne M, Behera S, Luo JJ, Cravatte S, Masson S, Yamagata T (2010) Influence of the state of the Indian Ocean Dipole on the following years El Niño. *Nat Geosci* 3:168–172
- Jin FF (1997) An equatorial ocean recharge paradigm for ENSO. Part I: conceptual model. *J Atmos Sci* 54(7):811–829
- Kennedy JJ, Rayner NA, Smith RO, Parker DE, Saunby M (2011a) Reassessing biases and other uncertainties in sea surface temperature observations measured in situ since 1850: 1. Measurement and sampling uncertainties. *J Geophys Res* 116(D14):D14103
- Kennedy JJ, Rayner NA, Smith RO, Parker DE, Saunby M (2011b) Reassessing biases and other uncertainties in sea surface temperature observations measured in situ since 1850: 2. Biases and homogenization. *J Geophys Res* 116(D14):D14104
- Kestin TS, Karoly DJ, Yano J, Rayner NA (1998) Time-frequency variability of ENSO and stochastic simulations. *J Clim* 11:2258–2272
- Kleeman R (2008) Stochastic theories for the irregularity of ENSO. *Philos Trans R Soc A* 366:2509–2524
- Kleeman R (2011) Spectral analysis of multi-dimensional stochastic geophysical models with an application to decadal ENSO variability. *J Atmos Sci* 68:13–25
- Kleeman R, Moore AM (1999) A new method for determining the reliability of dynamical ENSO predictions. *Mon Weather Rev* 127:694–705
- Kleeman R, McCreary J, Klinger B (1999) A mechanism for the decadal variation of ENSO. *Geophys Res Lett* 26:1743
- Kug JS, Sooraj K, Li T, Jin FF (2010) Precursors of the El Niño–La Niña onset and their interrelationship. *J Geophys Res* 115(D5). doi:10.1029/2009JD012861
- Latif M, Barnett T, Cane M, Fluegel M, Graham N, von Storch H, Xu JS, Zebiak S (1994) A review of ENSO prediction studies. *Clim Dyn* 9:167–179
- Lau NC (1997) Interactions between global SST anomalies and the midlatitude atmospheric circulation. *Bull Am Meteorol Soc* 78:21–33
- Lohmann K, Latif M (2005) Tropical Pacific decadal variability and the subtropical-tropical cells. *J Clim* 18(23):5163–5178
- van Loon H, Shea DJ (1985) The Southern Oscillation. Part IV: the precursors south of 15°S to the extremes of the oscillation. *Mon Weather Rev* 113:2063–2074
- van Loon H, Shea DJ (1987) The Southern Oscillation. Part VI: anomalies of sea level pressure on the southern hemisphere and of Pacific sea surface temperature during the development of a warm event. *Mon Weather Rev* 115:370–379

- Lukas R, Lindstrom E (1991) The mixed layer of the western equatorial Pacific ocean. *J Geophys Res* 96:3343–3358
- Mantua NJ, Hare SR, Zhang Y, Wallace JM, Francis RC et al (1997) A Pacific interdecadal climate oscillation with impacts on salmon production. *Bull Am Meteorol Soc* 78(6):1069–1080
- Mayer M, Trenberth KE, Haimberger L, Fasullo JT (2013) The response of tropical atmospheric energy budgets to ENSO. *J Clim* 26:4710–4724
- Meyers S, O'Brien J, Thelin E (1999) Reconstruction of monthly SST in the tropical Pacific ocean during 1868–1993 using adaptive climate basis functions. *Mon Weather Rev* 127(7):1599–1612
- Moore A, Kleeman R (1998) Skill assessment for ENSO using ensemble prediction. *Q J R Meteorol Soc* 124:557–584
- Newman M, Compo G, Alexander M (2003) ENSO-forced variability of the Pacific Decadal Oscillation. *J Clim* 16:3853–3857
- Penland C, Magorian T (1993) Prediction of Niño 3 sea surface temperatures using linear inverse modeling. *J Clim* 6:1067–1076
- Penland C, Sardeshmukh PD (1995) The optimal growth of tropical sea surface temperature anomalies. *J Clim* 8:1999–2024
- Percival DB, Walden AT (1998) Spectral analysis for physical applications: multitaper and conventional univariate techniques, 2nd edn. Cambridge University Press, Cambridge
- Power S, Casey T, Folland C, Colman A, Mehta V (1999) Interdecadal modulation of the impact of ENSO on Australia. *Clim Dyn* 15:319–324
- Rasmusson EM, Carpenter TH (1982) Variations in tropical sea surface temperature and surface wind fields associated with the Southern Oscillation/El Niño. *Mon Weather Rev* 110:354–384
- Rayner NA, Parker DE, Horton EB, Folland CK, Alexander LV, Rowell DP, Kent EC, Kaplan A (2003) Global analyses of sea surface temperature, sea ice, and night marine air temperature since the late nineteenth century. *J Geophys Res* 108(D14):4407. doi:10.1029/2002JD002670
- Smith TM, Reynolds RW (2004) Reconstruction of monthly mean oceanic sea level pressure based on COADS and station data (1854–1997). *J Oceanic Atmos Tech* 21:1272–1282
- Smith TM, Reynolds RW, Peterson TC, Lawrimore J (2008) Improvements to NOAA's historical merged land-ocean surface temperature analysis (1880–2006). *J Clim* 21:2283–2296
- Stephens DJ, Meuleners MJ, van Loon H, Lamond MH, Telcik NP (2007) Differences in atmospheric circulation between the development of weak and strong warm events in the Southern Oscillation. *J Clim* 20:2191–2209
- Stevens B, Giorgetta MA, Esch M, Mauritsen T, Crueger T, Rast S, Salzmann M, Schmidt H, Bader J, Block K, Brokopf R, Fast I, Kinne S, Kornbluh L, Lohmann U, Pincus R, Reichler T, Roeckner E (2013) Atmospheric component of the MPI-M Earth System model: ECHAM6. *J Adv Model Earth Syst* 5(2):146–172. doi:10.1002/jame.20015
- von Storch H, Zwiers FW (1999) Statistical analysis in climate research, 1st edn. Cambridge University Press, Cambridge
- von Storch H, Bruns T, Fischer-Bruns I, Hasselmann K (1988) Principal Oscillation Pattern analysis of the 30- to 60-day oscillation in general circulation model equatorial troposphere. *J Geophys Res* 93:11,022–11,036
- von Storch H, Buerger G, Schnur R, von Storch JS (1995) Principal Oscillation Patterns, a review. *J Clim* 8:377–400
- Thompson CJ, Battisti DS (2001) A Linear Stochastic Dynamical Model of ENSO. Part II: analysis. *J Clim* 14(4):445–466
- Thomson DJ (1982) Spectrum estimation and harmonic analysis. *Proc IEEE* 70:1055–1096
- Torrence C, Compo GP (1998) A practical guide to wavelet analysis. *Bull Am Meteorol Soc* 79:61–78
- Torrence C, Webster PJ (1999) Interdecadal changes in the ENSO—monsoon system. *J Clim* 12:2679–2690
- Trenberth K (1976) Spatial and temporal variations of the Southern Oscillation. *Q J R Meteorol Soc* 102:639–653
- Trenberth K, Shea DJ (1987) On the evolution of the southern oscillation. *Mon Weather Rev* 115:3078–3096
- Trenberth K, Branstator G, Karoly D, Kumar A, Lau NC, Ropelewski C (1998) Progress during TOGA in understanding and modeling global teleconnections associated with tropical sea surface temperatures. *J Geophys Res* 103(D08205):14,291–14,324
- Trenberth KE, Caron JM, Stepaniak DP, Worley S (2002) Evolution of El Niño Southern Oscillation and global atmospheric surface temperatures. *J Geophys Res* 107(D8). doi:10.1029/2000JD000298
- Tziperman E, Stone L, Cane MA, Jarosh H (1994) El Niño chaos: overlapping of resonances between the seasonal cycle and the Pacific ocean-atmosphere oscillator. *Science* 264:72–74
- Vimont DJ (2005) The contribution of the interannual ENSO cycle to the spatial pattern of decadal ENSO-like variability. *J Clim* 18:2080–2092
- Vimont DJ, Battisti DS, Hirst AC (2003a) The seasonal footprinting mechanism in the CSIRO general circulation models. *J Clim* 16:2653–2667
- Vimont DJ, Wallace JM, Battisti DS (2003b) The seasonal footprinting mechanism in the Pacific: implications for ENSO. *J Clim* 16:2668–2675
- Wang B, Wang Y (1996) Temporal structure of the southern oscillation as revealed by waveform and wavelet analysis. *J Clim* 9:1586–1598
- Wang H, Mehta VM (2008) Decadal variability of the Indo-Pacific warm pool and its association with atmospheric and oceanic variability in the NCEP-NCAR and SODA reanalyses. *J Clim* 21(21):5545–5565
- Weisberg RH, Wang C (1997) Slow variability in the equatorial west-central Pacific in relation to ENSO. *J Clim* 10(8):1998–2017
- Wheeler MC, Kiladis GN (1999) Convectively coupled equatorial waves: analysis of clouds and temperature in the wavenumber-frequency domain. *J Atmos Sci* 56:374–399
- Wu D, Anderson D, Davey M (1994) ENSO prediction experiments using a simple ocean-atmosphere model. *Tellus A* 46:465–480
- Wyrski K (1975) El Niño—the dynamic response of the equatorial Pacific ocean to atmospheric forcing. *J Phys Oceanogr* 5:572
- Xu JS, von Storch H (1990) Predicting the state of the Southern Oscillation using Principal Oscillation Pattern analysis. *J Clim* 3:1316–1329
- Yang GY, Hoskins B, Slingo J (2007) Convectively coupled equatorial waves. Part I: horizontal and vertical structures. *J Atmos Sci* 64:3406–3423
- Zebiak SE, Cane MA (1987) A model El Niño—Southern Oscillation. *Mon Weather Rev* 115:2262–2278
- Zhang Y, Wallace JM, Battisti DS (1997) ENSO-like interdecadal variability: 1900–1993. *J Clim* 10:1004–1020
- Živković T, Rypdal K (2013) ENSO dynamics: low-dimensional-chaotic or stochastic? *J Geophys Res* 118:2161–2168